Improving Rayleigh-Wave Dispersion Analysis in Glacial Ice Using Multi-Component Data

Journal:	*Journal of Glaciology*
Manuscript ID	JOG-2026-0029
Manuscript Type:	Article
Date Submitted by the Author:	06-Mar-2026
Complete List of Authors:	Garvey, Samara; Colorado School of Mines Siegfried, Matthew; Colorado School of Mines, Department of Geophysics Shragge, Jeff; Colorado School of Mines Zoet, Lucas; University of Wisconsin-Madison, Geoscience Hansen, Dougal; Washington University in St Louis Stevens, Nathan; University of Washington, Pacific Northwest Seismic Network
Keywords:	Glacier geophysics, Glaciological instruments and methods, Seismology, Ice thickness measurements
Abstract:	Seismic ice velocity estimates provide quantitative constraints on glacial systems, including ice thickness, englacial structure, and bedrock topography. Velocity modeling using active-source seismic is often challenged by sub-optimal surveys due to complex field logistics. This study provides a practical guide for leveraging three-component (3-C) receivers in glacial seismic surveys to constrain potentially heterogeneous ice velocities through Rayleigh-wave dispersion analysis. We combine vertical and horizontal-radial displacement information via a complex summation in the shot-gather domain, producing a combined-complex (CC) component. The CC dispersion panels improve the low-frequency picks in the positive-frequency range, where dispersion importantly reflects progradational particle motion interacting with the ice-bedrock interface. We demonstrate the CC approach on a limited-aperture 3-C dataset

collected on the Saskatchewan Glacier in the Canadian Rocky Mountains, supported by a series of synthetic studies that provide data-conditioning guidance and methodological intuition. We model Rayleigh-wave behavior in glacial stratigraphy to illustrate the sensitivities of radial displacement compared to traditional vertical-component waveforms, and to provide a general understanding of glacial-ice Rayleigh-wave behavior, which has not been fully explored in the literature. Our work thus provides practical strategies that complement CC-component dispersion analysis on glacial ice with limited geophones, enabling improved depth constraints from logistically limited surveys.

Improving Rayleigh-Wave Dispersion Analysis in Glacial Ice Using Multi-Component Data

Samara M. GARVEY,[1] Matthew R. SIEGFRIED,[1] Jeffrey SHRAGGE,[1] Lucas ZOET,[2] Dougal HANSEN,[3] Nathan T. STEVENS[4]

[1]*Department of Geophysics, Colorado School of Mines, Golden, 80401, CO, USA*

[2]*Department of Geoscience, University of Wisconsin–Madison, Madison, 53706, WI, USA*

[3]*Department of Earth, Environmental, and Planetary Sciences,*
Washington University, St. Louis, MO, 63130

[4]*Pacific Northwest Seismic Network, University of Washington, Seattle, WA, USA*

*Correspondence: Samara Garvey <somar@mines.edu>

ABSTRACT. Seismic ice velocity estimates provide quantitative constraints on glacial systems, including ice thickness, englacial structure, and bedrock topography. Velocity modeling using active-source seismic is often challenged by sub-optimal surveys due to complex field logistics. This study provides a practical guide for leveraging three-component (3-C) receivers in glacial seismic surveys to constrain potentially heterogeneous ice velocities through Rayleigh-wave dispersion analysis. We combine vertical and horizontal-radial displacement information via a complex summation in the shot-gather domain, producing a combined-complex (CC) component. The CC dispersion panels improve the low-frequency picks in the positive-frequency range, where dispersion importantly reflects progradational particle motion interacting with the ice-bedrock interface.

We demonstrate the CC approach on a limited-aperture 3-C dataset collected on the Saskatchewan Glacier in the Canadian Rocky Mountains, supported by a series of synthetic studies that provide data-conditioning guidance and methodological intuition. We model Rayleigh-wave behavior in glacial stratigraphy to illustrate the sensitivities of radial displacement compared

to traditional vertical-component waveforms, and to provide a general understanding of glacial-ice Rayleigh-wave behavior, which has not been fully explored in the literature. Our work thus provides practical strategies that complement CC-component dispersion analysis on glacial ice with limited geophones, enabling improved depth constraints from logistically limited surveys.

INTRODUCTION

The structure and material properties of ice masses and underlying bedrock are key parameters that control ice flow (e.g., Bennett, 2022). Active-source seismic methods, which operate at low (sub-200 Hz) frequencies (Podolskiy and Walter, 2016), allow for deep subsurface investigations (e.g., at the ice-bedrock interface and internal bedrock layering) by using a controlled source of acoustic waves, which are sensitive to variations in compressional- (P) and shear- (S) wave velocities and density of the elastic medium. This method has been leveraged to map subglacial structures across multiple glacier types (typically using reflected or refracted wave data), such as at Rutford Ice Stream in West Antarctica (Smith, 1997) and the Taku (Zechmann and others, 2018) and Lemon Creek (Veitch and others, 2021) glaciers in Alaska. Active-source seismic methods are also able to resolve englacial heterogeneity in elastic properties where recorded frequencies are sufficiently high. Examples include mapping a shallow, 40 m englacial conduit at Rhonegletscher with a dominant frequency of 100 Hz (Church and others, 2019), mapping debris layers at Sourdough rock glacier in Alaska (Kuehn and others, 2024) with a 100 Hz dominant frequency, and building a seismic-velocity profile through the upper 80 m of firn at Korff Ice Rise in West Antarctica using a dominant frequency of 200 Hz (Agnew and others, 2023).

Typically, a two-dimensional (2-D) seismic survey is sufficient for estimating elastic velocities from which bedrock topography and ice thickness can be calculated. When source-receiver offset distances are long relative to the bedrock depth (i.e., $> 3\times$), refracted P-wave energy can be used to constrain P-wave velocity models (V_p) at depth (e.g., Redpath, 1973). For more limited-offset surveys, Rayleigh waves that propagate along the surface of the Earth and are reliably strong signals (e.g., Richart and others, 1970; Socco and Strobbia, 2004; Picotti and others, 2015) can be used to constrain S-wave velocity (V_s) depth profiles (Crice, 2005). Active-source experiments on glaciers are often offset-limited due to the logistical challenges of operating on ice (Aster and Winberry, 2017), which suggests that Rayleigh-wave methods should be well suited for glacial experiments.

V_s-modeling using Surface Rayleigh Waves

There are two common approaches for deriving elastic model properties from Rayleigh waves. The first is the horizontal-to-vertical spectral ratio (HVSR) method, which, although it reflects contributions from multiple wave modes, specifically represents the elliptical particle motion of Rayleigh waves (e.g., Mi and others, 2019; Abdialim and others, 2021). The second approach is the multi-channel analysis of surface waves (MASW), which exploits the dispersive nature of Rayleigh waves (i.e., the change in phase velocity, V_r, with frequency, f) to extract elastic properties of the subsurface.

The HVSR approach estimates a bulk thickness of the ice, h, from the resonant frequency (f_0) of ambient Rayleigh-wave energy recorded on a seismic array in conjunction with a V_s estimate that is typically derived from P-waves recorded on a co-located active-seismic survey and an empirical V_p/V_s ratio. We refer the reader to Picotti and others (2017) and Preiswerk and others (2019) for seminal applications of HVSR in glacier settings. Stevens and others (2023), for example, applied this workflow to a dataset acquired on the Saskatchewan Glacier in the Canadian Rocky Mountains, intially using an "accepted" $V_p/V_s = 1.95$, with subsequent refinement to 1.93 in a follow-on study (Stevens and others, 2024).

In its simplest implementation, the HVSR method assumes a planar-layer-over-half-space model from which the upper layer thickness (which in this case is ice thickness, h) can be estimated as $h = \frac{V_s}{4f_0}$ (Ibs-von Seht and Wohlenberg, 1999). Picotti and others (2017) critically discusses several limitations of this approach, noting that when the rigid half-space assumption breaks down — for example, in the presence of soft, water-saturated bedrock or low-velocity englacial heterogeneity — thickness estimates may be biased. Additionally, thick firn layers can attenuate or modify the ambient wavefield associated with the ice–bed interface, and in thin glaciers, resonance occurs at higher frequencies where ambient noise sources are more variable, leading to reduced temporal stability in HVSR curves. In multi-layered environments, the core assumption of a planar layer over a stiffer half-space — upon which estimates of h are based (Koller and others, 2004) — is further violated. Although regularized inversion of the full HVSR curve has demonstrated success in resolving multi-layer structure and lateral variability in many geotechnical applications (e.g., Bignardi and others, 2016), the inversion remains weakly constrained without independent information on V_s. Consequently, thickness estimates may be geologically unrealistic. These limitations of the HVSR method underscore the need for velocity model-building approaches that minimize reliance on empirical relationships and provide independent constraints on shear-wave velocity.

MASW is one such approach, as it avoids the uncertainties associated with the two-layer assumptions underlying HVSR and directly provides Rayleigh-wave velocity information from which V_s constraints can be inferred. It is typically implemented in active-source experiments and is especially effective for analyzing higher-frequency surface waves that probe shallower depths than those typically estimated by HVSR analysis. The method leverages the fact that Rayleigh waves are dispersive in a horizontally layered medium — their phase velocity varies with frequency because different frequencies sample different depths. The observed frequency-dependent Rayleigh-wave velocity, $V_r(f)$, is strongly controlled by the near-surface shear-wave velocity structure (V_s), and therefore can be inverted to estimate $V_s(z)$.

Developed by Park and others (1999), MASW is widely used in geotechnical engineering (e.g., Crice, 2005) for soil characterization, though it also finds applications in permafrost characterization in periglacial settings (e.g., Glazer and others, 2020; Tourei and others, 2024) and hard-rock characterization for mineral exploration and mine planning (Papadopoulou, 2021). Its popularity stems from its near-surface sensitivity and its applicability to conventional seismic refraction line data, providing additional utility without requiring a separate survey. The MASW workflow is also relatively straightforward and accessible through open-source software such as *MASWaves* (Olafsdottir and others, 2018).

A significant limitation of MASW is that the resulting $V_r(f)$ trend, herein referred to as the dispersion curve (DC), provides an averaged view of the subsurface between the furthest receiver and the shot point, effectively reducing a 2-D setting to a 1-D profile and assuming lateral homogeneity beneath the array (thus ignoring localized crevassing or englacial water systems or pronounced structural relief). V_s layering can also generate higher-order modes (harmonics) with unique dispersion characteristics that may interact with the fundamental mode, making it more difficult to distinguish between dispersive modes. Even once a practitioner has picked the DC to the best of their ability, inversion remains challenging because the relationship between $V_r(f)$ and $V_s(z)$ is non-unique (Foti and others, 2018). As a result, both the forward problem of constructing the DC and the inverse problem are equally important in determining the clarity of the dispersion image and the confidence with which the final velocity structure can be interpreted.

In glacial settings, the challenges of the forward problem are amplified by logistical constraints, such as limited receiver counts or the need for low-impact sources during weight-restricted field expeditions, which helps explain its more limited utility compared to other domains of application. For example, at Sourdough rock glacier, Alaska, Kuehn and others (2024) used only 12 vertical-component (1-C) geophones at 5 m spacing, which allowed accurate seismic velocity estimates for just the upper 5 m of the ice column. In contrast, at Spitsbergen in the Norwegian Arctic, MASW was used to constrain a deep subglacial low-velocity zone down to 200 m, but this required a longer receiver array (1500 m) with 60 1-C geophones deployed at 25 m spacing, combined with higher-mode dispersion analysis (Tsuji and others, 2012).

It is worth noting that in passive applications focused on broadband characterization, acquisition constraints are less restrictive, and dispersion analysis is well suited for measuring bulk ice-sheet thickness (e.g., Lawrence and others, 2006; Walter and others, 2015). Zhang and others (2022) demonstrated its application to mapping low-frequency trends in firn seismic velocity with depth, with the caveat that, as Qin and others (2024) show, the resolution achieved in Zhang and others (2022) is generally consistent with their HVSR results. Consequently, dispersion analysis is uniquely valuable in active-source experiments, as it can supplement passive HVSR approaches by providing higher-resolution insights.

Only a handful of authors have focused on optimizing active-source MASW for glacial characterization. These include: Ivanov and others (2016), who investigated velocity solutions constrained by density in the inversion; Picotti and others (2015), who used both Rayleigh and Love waves recorded on 3-C data to separately invert for SV and SH profiles and interpret vertically-transverse isotropy from travel-time inversion of diving waves; and Killingbeck and others (2018), who considered a trans-dimensional Bayesian inversion framework to overcome solution non-uniqueness. These approaches primarily focus on optimizing the inversion itself and do not directly address the limitations imposed by the quality and coverage of the input data — a gap that our study seeks to fill by leveraging multi-component data.

Multi-Component Analysis of Rayleigh Wave Signal

As Rayleigh-wave particle motion is elliptical, the wavefield contains both vertical and horizontal displacement. This idea underpins HVSR, but it also creates an opportunity for improving dispersion analysis since the vertical and in-line horizontal channels of three-component (3-C) geophones both record Rayleigh-wave energy. When these gathers are transformed into a $V_r - f$ image (herein referred to as a dispersion panel, DP), one would expect the picked DCs to be similar because both components respond to the same Rayleigh-wave energy propagating with a shared theoretical phase velocity V_r. However, practitioners who have examined multi-component Rayleigh-wave dispersion have reported that the resulting energy spectra often differ. Ikeda and others (2015) suggest that this arises from how the relative strengths of vertical and horizontal motion change with frequency and with the subsurface structure. Dal Moro and others (2015) further note that the source type also influences these differences, making it difficult to anticipate which component will yield a clearer image for dispersion picking in a given setting. Boaga and others (2013) suggest that comparing vertical and horizontal components can help separate modes at “kissing” frequencies — where modal trends approach each other —especially in low-velocity zones where the fundamental-mode energy is reduced on the vertical component.

Where practitioners have attempted to use both components, they typically generate dispersion panels from each component separately, then either pick and average the dispersion curves (Picotti and others, 2015; Calderón-Macías and Simmons, 2008) or stack the dispersion panels and pick the dispersion curve (Pan and others, 2018). Dal Moro and others (2017) proposed a unique approach by examining Rayleigh-wave particle motion through frequency-dependent correlation coefficients between the inline-horizontal component and the Hilbert transform of the vertical component, jointly inverting these along with the vertical and inline-horizontal dispersion curves. Sun and others (2022) present a method for computing a rotational component that shows strong performance in synthetic experiments. However, extending this formulation to field data may require additional considerations, since direct calculation of the curl is not generally feasible with standard acquisition geometries.

Qiu and others (2019) combine two components of ground motion into a single complex-valued quantity to analyze surface waves. In their formulation, the vertical component is treated as the imaginary part of the complex expression. They apply this approach to shallow soils and focus on evaluating higher-order wave modes.

We adopt a similar complex summation strategy but define the components differently. In our formulation, the radial component is treated as the imaginary part of the complex quantity, which aligns the representation with the underlying particle motion and provides an intuitive way to analyze the positive and negative frequencies of the dispersion analysis. As opposed to Qiu and others (2019), our application focuses on glacial environments and primarily targets the fundamental mode of surface waves, which is typically the most energetic and stable component of the signal. In addition, building on theory that has not previously been evaluated in practice, we demonstrate the importance of careful data conditioning within the complex-summation workflow. This step proves critical for obtaining stable and interpretable dispersion images, including both negative- and positive-frequency panels.

To arrive at these insights, we present the analysis in a stepwise manner. We begin by outlining the modeling and coordinate framework assumptions underlying our work, followed by an overview of

Rayleigh-wave theory relevant to leveraging multi-component (MC) data in MASW. Before introducing MC-MASW, we contrast Rayleigh-wave propagation in ice with that in other commonly studied elastic media, establishing the key assumptions and motivations for glacial applications. We then describe our approach and demonstrate it using a synthetic example representing an ice-over-bedrock system. Finally, we apply MC-MASW to an aperture-limited dataset acquired on the Saskatchewan Glacier (Stevens and others, 2023). We conclude by offering practical recommendations for MC data acquisition, preprocessing, and Rayleigh-wave dispersion analysis in glacial investigations.

THEORETICAL FRAMEWORK

We focus our case studies on the 2-D problem in the x–z plane of wave propagation, restricting the synthetic experiments to isotropic, linear elastic solids. Accounting for anisotropy is a natural extension of this work, particularly given that ice is generally considered anisotropic (e.g., Aster and Winberry, 2017; Diez and Eisen, 2015; Faria and others, 2014).

In all analyses, we assume an acquisition coordinate system where the vertical (z) axis is positive downward and the horizontal (x) axis is oriented along the 2-D array. In practical terms, this means the horizontal components of the geophones are oriented in the x and y directions (Figure 1a). However, because our focus is on Rayleigh waves—which, by this coordinate definition, propagate in the x-z plane—we do not consider the y-component data, although it becomes important when investigating Love waves.

For field experiments with non-uniform geophone orientations or multi-azimuth acquisitions with directional (signed) offsets, rotating the recorded data into a radial-transverse (R-T) coordinate system is a critical preprocessing step to isolate azimuthal variations in particle displacement (Gaiser, 1999). The R and T components point along and perpendicular to the source-receiver azimuth, respectively (Fig. 1b), separating Rayleigh and Love wave energy.

In the synthetic experiments of this manuscript, we model only positive offsets, with the source positioned to the left of the receivers. Thus, all horizontal-component data are oriented along the positive x direction (e.g., receiver G2 in Fig. 1a), corresponding to the R component (e.g., receiver G2 in Fig. 1b).

GENERAL THEORY OF RAYLEIGH WAVE BEHAVIOR

Rayleigh waves form near the surface of an elastic medium due to the post-critical incidence of SV-body waves on the free surface (in this case, the air-ice interface). This interaction generates evanescent P- and

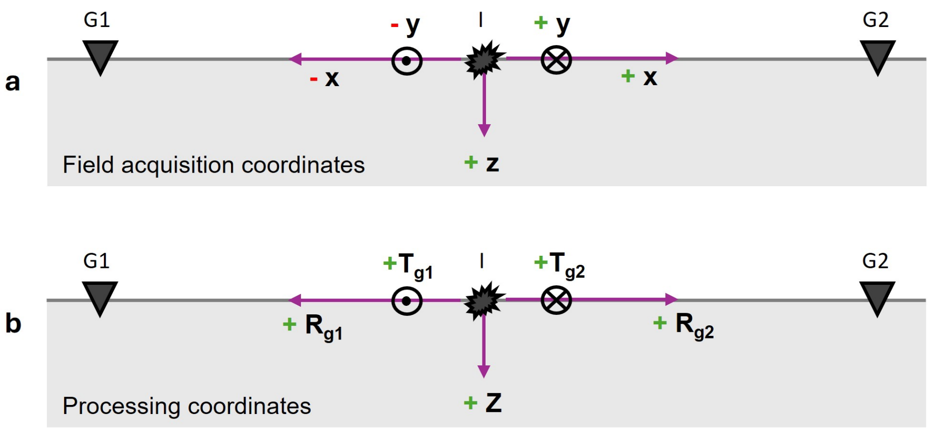

Fig. 1. Definition of the (a) acquisition coordinate system in horizontal x and y and vertical z directions, and (b) the cylindrical processing coordinate system in outward-positive radial R and vertical Z directions. The transverse, T direction is always counter clockwise from R. I and G annotate the locations of the impact source and receivers, respectively, in each sketch.

SV-wavefields that are 90° out of phase (Lay and Wallace, 1995; Liner, 2012), producing the characteristic elliptical particle motion of Rayleigh waves that propagate along the surface (Lay and Wallace, 1995; Liner, 2012). Supplementary Material Text S1 provides additional detail on this process and shows how the vertical (U_z) and horizontal (U_x) displacements of the elliptical motion can be represented as sums of spatial derivatives of the evanescent wavefields. For the purposes of building intuition for the Rayleigh wavefield, we simplify the discussion by assuming an isotropic, homogeneous Earth system, where U_x and U_z (as shown in Fig. S1.1) can be expanded as:

$$U_x = -A\omega p \sin\left(\omega(px - t)\right)\left[\mathrm{e}^{-\omega\hat{\eta}_p z} + \frac{1}{2}\left(\frac{{V_r}^2}{V_s^2} - 2\right)\mathrm{e}^{-\omega\hat{\eta}_s z}\right], \tag{1}$$

and

$$U_z = -A\omega p \cos\left(\omega(px - t)\right)\left[V_r\hat{\eta}_p\mathrm{e}^{-\omega\hat{\eta}_p z} + \frac{1}{V_r\hat{\eta}_s}\frac{1}{2}\left(\frac{{V_r}^2}{V_s^2} - 2\right)\mathrm{e}^{-\omega\hat{\eta}_s z}\right]. \tag{2}$$

These displacements are a product of three terms: (1) amplitude terms dependent on the angular frequency ω, the horizontal slowness p of the Rayleigh wave, and a scaling constant A; (2) time-dependent terms describing harmonic plane-wave motion along the x direction (note cosine versus sine functions in U_z and U_x, respectively, which generates the 90° phase difference); and (3) terms specifying amplitude decay with depth (z) dependent on vertical slownesses of the evanescent P- and SV-waves ($\hat{\eta}_p$ and $\hat{\eta}_s$ respectively).

We focus on the third terms of Equations (1) and (2) within "[ ]" brackets, as they encapsulate the dependence of Rayleigh-wave displacement on subsurface V_s structure. This includes properties such as ellipticity, particle motion direction, and the depth-dependent sensitivity of amplitude. These terms are eigenfunctions for which the Rayleigh-wave phase velocity V_r is the eigenvalue (Aki and Richards, 2002). This is an important feature, as it provides a means of solving for V_r using the characteristic equation derived by combining U_z and U_x through the free-surface boundary condition (Lay and Wallace, 1995). The characteristic equation relates V_r, which is defined along the vector direction of the elliptical particle motion, to the V_s of the subsurface. Before exploring this concept, we first contrast Rayleigh-wave propagation characteristics in ice with those in other elastic media to establish the key assumptions and motivations for glacial applications of MC-MASW.

Glacial Ice Compared To Other Elastic Materials

The goal of this section is to address a gap in the glaciology literature by examining Rayleigh-wave responses in glacial ice characterized by stronger contrast layering and different elastic relationships compared to commonly studied soils and Poisson-solid-like hard-rock materials. This provides an important foundation for advancing MC-MASW in glacial applications and for validating assumptions when applying concepts developed for other elastic media.

This analysis focuses on the homogeneous isotropic half-space model, where the Rayleigh-wave characteristic equation simplifies to

$$\frac{V_r^6}{V_s^6} - 8\frac{V_r^4}{V_s^4} + \left(24 - 16\frac{V_s^2}{V_p^2}\right)\frac{V_r^2}{V_s^2} + 16\left(\frac{V_s^2}{V_p^2} - 1\right) = 0. \tag{3}$$

The solution of V_r from the characteristic equation is often constrained by realistic V_p/V_s ratios. We illustrate this constraint by plotting V_r/V_s as a function of V_p/V_s (Fig. 2) and comparing several glacial estimates (Table 1) derived from published studies with those of a Poisson solid (Ammon and others, 2020) and fully saturated soil (Yang, 2005), also listed in Table 1. We observe that the glacial estimates of V_r/V_s are slightly higher than for a Poisson solid but significantly lower than for fully saturated soil, and that the V_p/V_s ratios for glacial ice are closer to that of a Poisson solid than typical soil profiles.

It is well understood that the Rayleigh-wave particle motion is retrograde at the free surface and transitions to prograde at a depth h_r, where $U_x = 0$; that is, the shallowest depth at which the third term of Equation (2) becomes zero (Ammon and others, 2020; Aki and Richards, 2002). The depth h_r can be

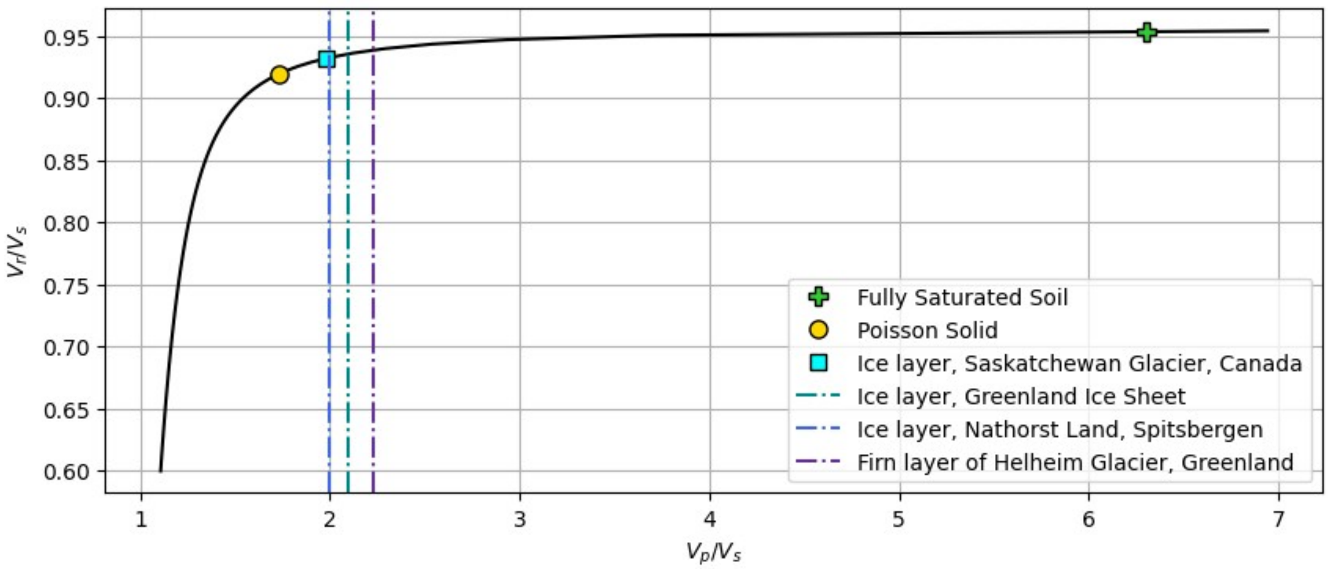

Fig. 2. Homogeneous, isotropic, Rayleigh-wave characteristic equation (Equation. (3)) represented as a relationship between V_p/V_s and V_r/V_s (black curve) with reference values for a saturated soil (green cross), Poisson solid (yellow circle), and glacial ice at the Saskatchewan Glacier (cyan square). V_p/V_s estimates of other glacial examples are plotted as vertical lines since V_r/V_s estimates are not mentioned in reference studies. Table 1 lists associated material properties.

Table 1. Elastic properties for different subsurface media examined in our analytical models: a. fully saturated soil profile (Yang, 2005); b. Poisson solid (Ammon and others, 2020); c1. ice layer derived from the Saskatchewan Glacier (Stevens and others, 2023); c2. ice layer derived from the Greenland Ice Sheet (Walter and others, 2015); c3. ice layer derived from Nathorst Land, Spitsbergen (Johansen and others, 2011); d. firn layer derived from Helheim Glacier, Greenland (Killingbeck and others, 2020). Note that although some case studies report higher-precision values, we have rounded results to the nearest hundredth for consistency.

	Model	V_p (m s^{-1})	V_p/V_s	V_r/V_s
a	Fully Saturated Soil	1550	6.30	0.95
b	Poisson Solid	5800	1.73	0.92
c1	Ice (Saskatchewan Glacier)	3450	1.95	0.93
c2	Ice (Greenland Ice Sheet)	3870	2.10	—
c3	Ice (Spitsbergen)	3600	2.00	—
d	Firn (Helheim Glacier)	2900	2.23	—

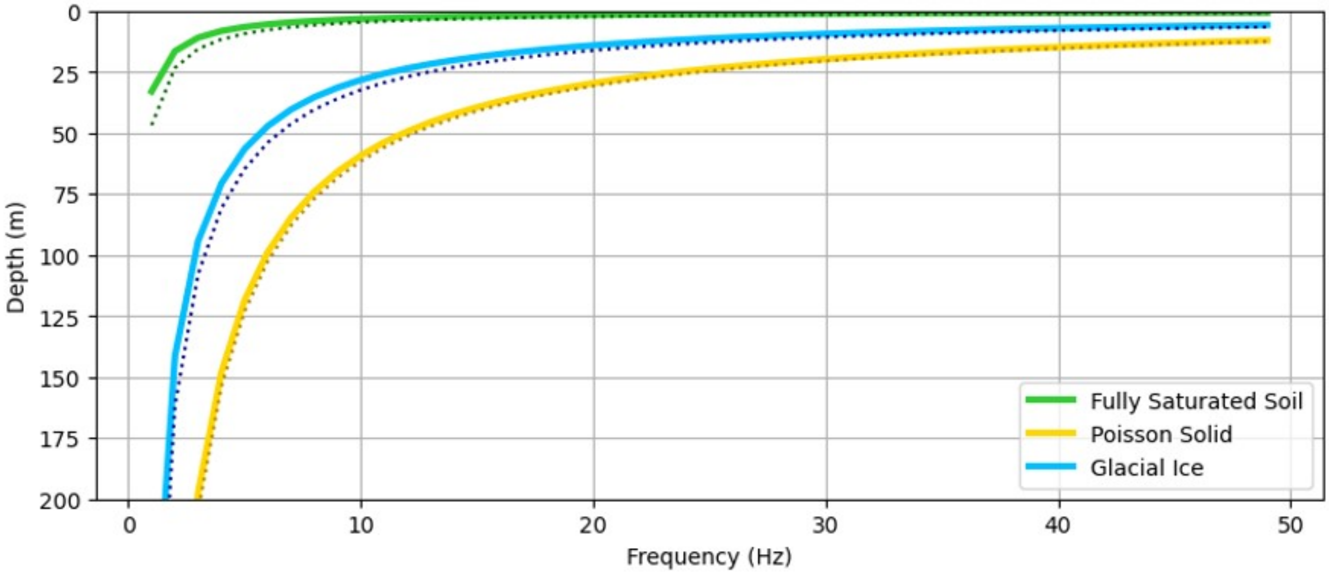

Fig. 3. Frequency-dependent depths at which Rayleigh-wave particle motion change from retrograde to prograde for a fully saturated soil profile (green) (Yang, 2005), a Poisson's solid (yellow) (Ammon and others, 2020), and glacial ice (blue) based on parameters estimated for the Saskatchewan Glacier (Stevens and others, 2023). Solid line are analytical solutions (Equation (4)), and dotted lines are approximated depths based on $\frac{1}{5}\lambda$ for all models. 1 lists associated material properties.

calculated analytically as

$$h_r = \frac{\ln\left(1 - \frac{V_r^2}{2V_s^2}\right)}{\omega\left(\hat{\eta}_s - \hat{\eta}_p\right)}, \tag{4}$$

or is often approximated as $\frac{1}{5}$ of the dominant wavelength, λ where $\lambda = V_r/f$ (Ammon and others, 2020). We validate that this general expression holds for glacial ice in Fig. 3 by comparing the analytical and rule-of-thumb solutions for the Saskatchewan Glacier cited in Table 1, along with that of the Poisson solid and saturated soil profile described in Table 1.

Layering and Dispersion Effects

In a layered Earth, the Rayleigh-wave displacement and characteristic equations (Equations (1), (2), and (3)) become more complex than homogeneous scenarios and require numerical solutions (Aki and Richards, 2002). This is due to the relationship between V_r and f that introduces dispersive behavior. For example, in an Earth model where elastic velocities increase with depth, lower-frequency modes that penetrate deeper will sample faster velocities and therefore travel with faster phase velocities than the higher-frequency wave-mode components. We refer the reader to Ammon and others (2020) for a comprehensive physical overview of dispersion phenomenon and to Aki and Richards (2002) for more advanced mathematical treatment.

Subsurface layering can act as waveguides that increase propagating wavefield complexity and cause waves to reflect and refract within these layers. However, only at certain frequencies will waves propagate in a manner that produces coherent and stable oscillations, which manifest as higher-order modes. The limiting frequencies over which a higher-order mode exists are a function of layer thickness, depth, velocity contrasts, and propagating frequencies. The modes are distinguishable by their different dispersive behavior and dominant frequency ranges. Higher-order modes are particularly important for recovering complex models with velocity inversions (i.e., where a fast velocity material overlies a slow velocity medium). A low-velocity layer will bend the transmitted ray toward the normal and allow for high-frequency oscillations within this layer. Multi-modal analysis can be necessary for characterizing voids or unfrozen layers (e.g., at Spitsbergen in the Norwegian Arctic; Tsuji and others, 2012) or firn-aquifer systems (e.g., at the Helheim Glacier in Greenland; Killingbeck and others, 2018).

Our analyses focus on the fundamental mode for two practical reasons. First, in a layer-over-half-space structure typical of many glaciological settings, the fundamental mode dominates the recorded amplitudes and therefore provides the most stable constraint on large-scale velocity structure. Second, because the goal of this work is to understand how multi-component measurements can improve Rayleigh-wave analysis in glacial ice, we intentionally isolate the most straightforward case before extending to more complex multi-mode behavior. This allows us to evaluate the added value of multi-component data without the compounding challenges of higher-order mode identification and analysis.

EXPLORING MULTI-COMPONENT RAYLEIGH WAVE SIGNALS

To explore how Rayleigh-wave energy appears on different displacement components, we begin with a simple synthetic experiment modeling a homogeneous ice over bedrock. Our synthetic experiment simulates a 2-D active-source survey using the open-source SOFI2D seismic modeling package (Bohlen and others, 2016). We emphasize that the purpose of this synthetic experiment is not to replicate exact field waveforms but to create a controlled, idealized scenario that allows clear analysis of dispersion characteristics.

The source is an explosive source represented by an Ormsby wavelet with a flat spectrum between 5 Hz and 200 Hz. The source and receivers are positioned slightly below the free surface (i.e., at 0.5 m) to reduce numerical modeling artifacts. Since resolution and accuracy of dispersion analysis is strongly shaped by acquisition parameters (Foti and others, 2018), we minimize their impact by mimicking an idealistic acquisition: a 1000 m receiver line with sensors spaced every 1 m.

The ice-over-bedrock model consists of a 100 m ice layer, representative of a median glacier thickness based on observations from the global catalog of glacial thickness assessments in Millan and others (2022). The modeled ice layer assumes values of $V_p = 3500$ m s^{-1}, $V_p/V_s = 2$, and density $\rho = 917$ kg m^{-3}, whereas the underlying bedrock half-space has $V_p = 4300$ m s^{-1}, $V_s = 2150$ m s^{-1}, and $\rho = 2600$ kg m^{-3}.

Fig. 4a and 4b show the corresponding Z- and R-component shot gathers, respectively, in wiggle-plot format, where every 100th trace is plotted for visual clarity. The Rayleigh-wave energy is dominant arrival on both components, with a slightly stronger expression on the Z component. A 90° phase rotation is present between the Z- and R-component Rayleigh-wave arrivals for all offsets (illustrated in Fig. 4c, which zooms in on the traces at 100 m offset). This observation is consistent with the expected phase offset between the vertical and horizontal displacements of the elliptical Rayleigh-wave particle motion (reference Equations 1 and 2).

To visualize dispersion in an active-source experiment, shot gathers are transformed into displays of relative signal amplitude in V_r-f space, and dispersion curves are identified by following the high-amplitude ridges. The detailed workflow used to generate these dispersion panels (DPs) is provided in Supplementary Material Text S2 to emphasize that no assumptions are made about whether the input is from the vertical- or horizontal-displacement components. Because both components are processed identically, this provides a basis for examining how differences between dispersion plots may offer complementary sensitivity to subsurface velocity layering and/or data conditioning and/or acquisition parameters.

Fig. 5a and 5b present the Z- and R-component DPs, respectively, generated from the raw gathers shown in Fig. 4. Because this is an idealized synthetic case, the raw data inherently produce reasonable DPs. However, we also include DPs generated after conditioning the data (Fig. 5c, 5d) by muting the direct wave and windowing out near-offset traces where muting interfered with the Rayleigh signal. For these idealized, noise-free synthetics, the most critical processing step is the correct removal of direct-wave energy from the R-component data which strongly affects the low frequency DC picks. We return to this point when introducing the CC approach to processing MC datasets (Section: The CC-Component) and again, with greater emphasis, in the field experiment (Section: Field Example of CC-component Analysis).

Although the data bandwidth extends beyond 50 Hz, we plot the DPs only up to this frequency because, above it, the fundamental-mode DC flattens and provides little information about the ice-bedrock interface. The resulting dispersion images generally recover the same fundamental-mode trend with differences

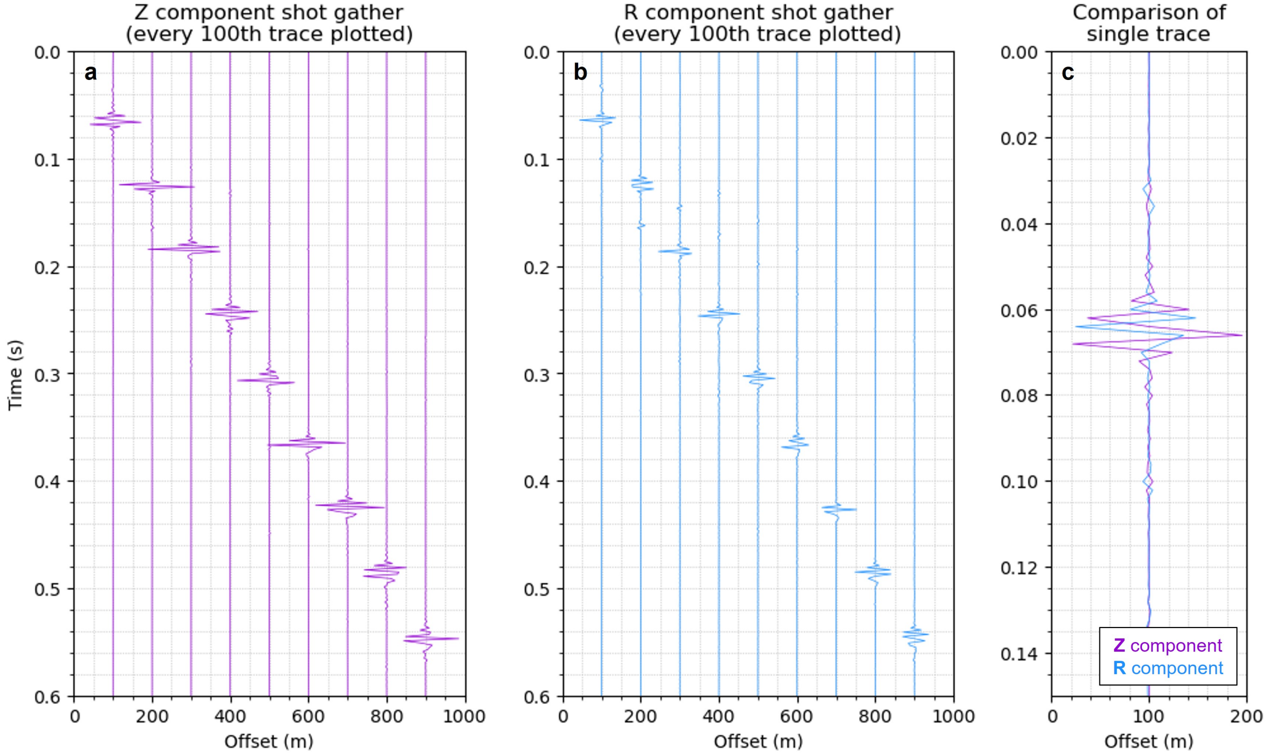

Fig. 4. Raw shot gathers comparison for an ice-over-bedrock half-space experiment showing the (a) Z- and (b) R-component traces plotted every 100th trace. (c) Comparison of Z and R traces at 100 m offset. The Rayleigh-wave energy is strong on both components, and the expected 90° phase difference is observed.

observed primarily in the range $8-15$ Hz (yellow boxed region in Fig. 5). The interpreted DC picks ('x's in Fig. 5) align well with the numerical solution (red dashed line in Fig. 5) in both plots. Although the Z component exhibits a strong distinct amplitude at 10 Hz, the R component arguably preserves a more uniform low-frequency trend.

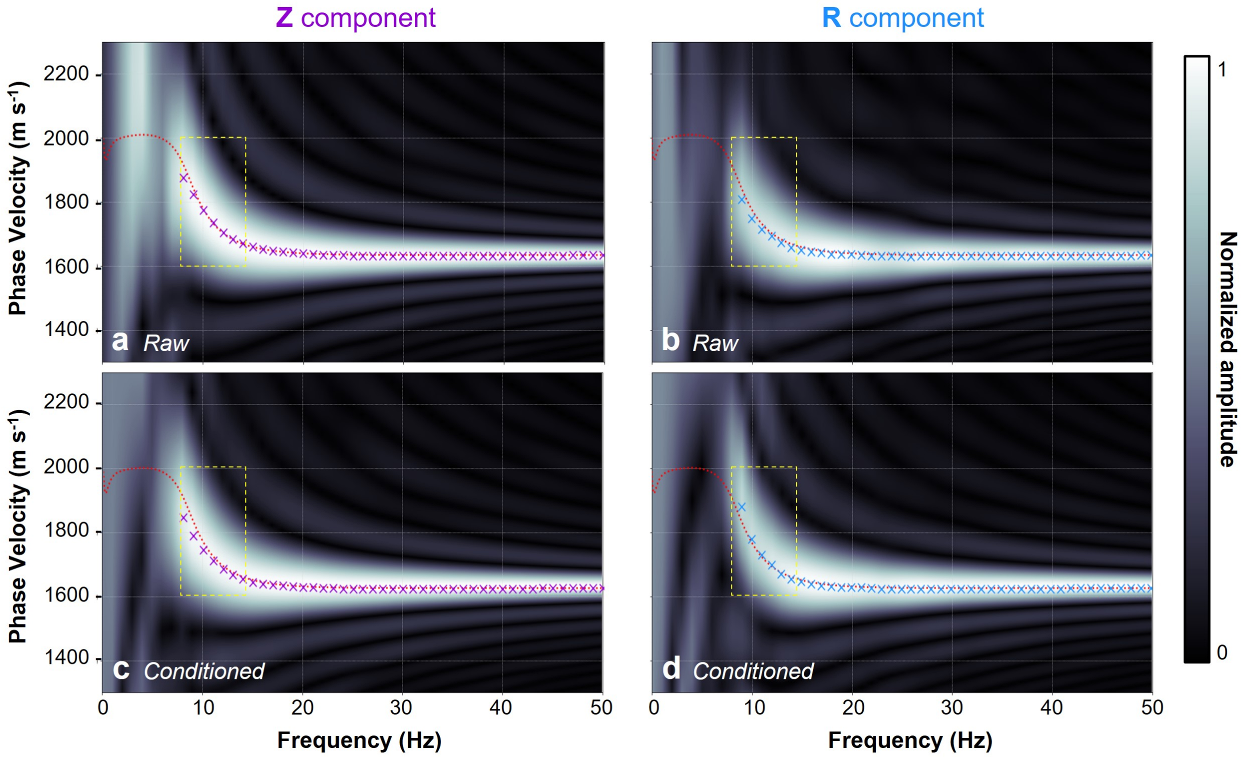

Fig. 5. Comparison of the (a) *Z*- and (b) *R*-component DPs generated from the raw gathers and (c, d) after applying data conditioning to mute the direct wave and window out affected near-offset traces. The numerical solution of the true dispersion curve (DC) is shown in red, and the automated DC picks (from *MASWaves*) are plotted as ‘x’s. Even though the synthetic data are noise-free and densely sampled, the conditioning has a noticeable effect — particularly on the low-frequency content of the *R* component — which leads to subtle but meaningful differences in the resulting DPs and DC picks of the combined-complex (*CC*) approach.

Depth-Sensitivity Kernels

We now examine the depth-sensitivity kernels of U_z and U_x to understand the utility of low-frequency content and the reasons for the observed differences in the low-frequency DCs between Z and R. These kernels illustrate how each component responds to velocity structure at depth by plotting the numerically calculated normalized eigenfunctions of U_z and U_x, which correspond to heterogeneous model extensions of the the third terms in Equations (1) and (2) for homogeneous media.

For reference, we compare the ice-over-bedrock half-space to an infinitely deep homogeneous ice column, which may represent scenarios where seismic depth-sensitivity is insufficient to detect subglacial material. The ice properties for the infinite-ice model match those used for the ice-bedrock model. The comparison of phase and group velocities for both models are shown in Fig. 6. Dispersion in the ice-bedrock model causes these velocities to diverge, and this separation reaches its maximum at 8.8 Hz in this case with 100 m thick ice in the ice-over-bedrock half-space model.

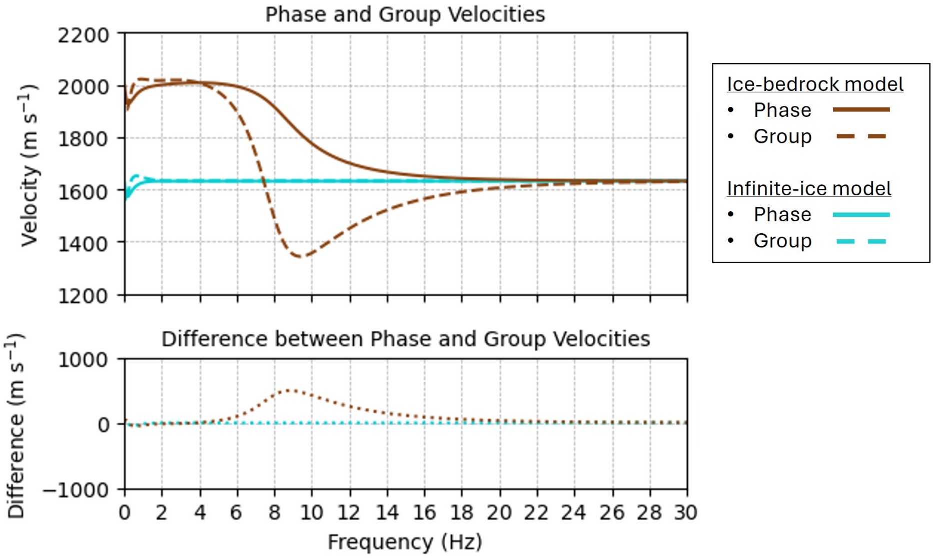

Fig. 6. Comparison of numerical solutions for Rayleigh wave group and phase velocities for the infinite-ice model (blue) and ice-over-bedrock half-space model (brown). There is no observed dispersion in the infinite-ice model as expected. Dispersion in the ice-bedrock model causes these velocities to diverge, with the greatest separation occurring at 8.8 Hz.

The U_x and U_z depth-sensitivity kernels for both models are shown in Fig. 7a–7f for discrete frequencies 7.0, 8.0, 9.0, 10.0, 20.0, and 30.0 Hz. The $7.0 - 10.0$ Hz range is selected to examine these kernels where dispersive signature of the ice-bedrock model is strongest based on Fig. 6. For both models, the horizontal displacements (dashed curves) are largest near the surface and are negative, indicating retrograde particle motion. For all frequencies examined, the infinite-ice model exhibits a single reversal to progradational motion (identified where $U_x = 0$) at approximately $\frac{1}{5}\lambda$, consistent with Equation (4). For the ice-over-bedrock model, frequencies above 8.8 Hz exhibit a similar depth of reversal, but this behavior differs at lower frequencies. At 7.0 and 8.0 Hz, the ice-bedrock model shows three reversal points: one near $\frac{1}{5}\lambda$ and two more located just above and just below the 100 m interface.

These observations highlight an important nuance in the depth-of-reversal assumption when a strong subsurface contrast is present at low frequencies. Although such effects are typically negligible in most soil studies where velocity gradients are gradual, they may play a more influential role in glacial environments. Of additional note is that the kernels for the ice-bedrock model also display a distinct inflection at the interface itself, with the expression of this feature being strongest at lower frequencies likely because higher frequencies probe shallower depths.

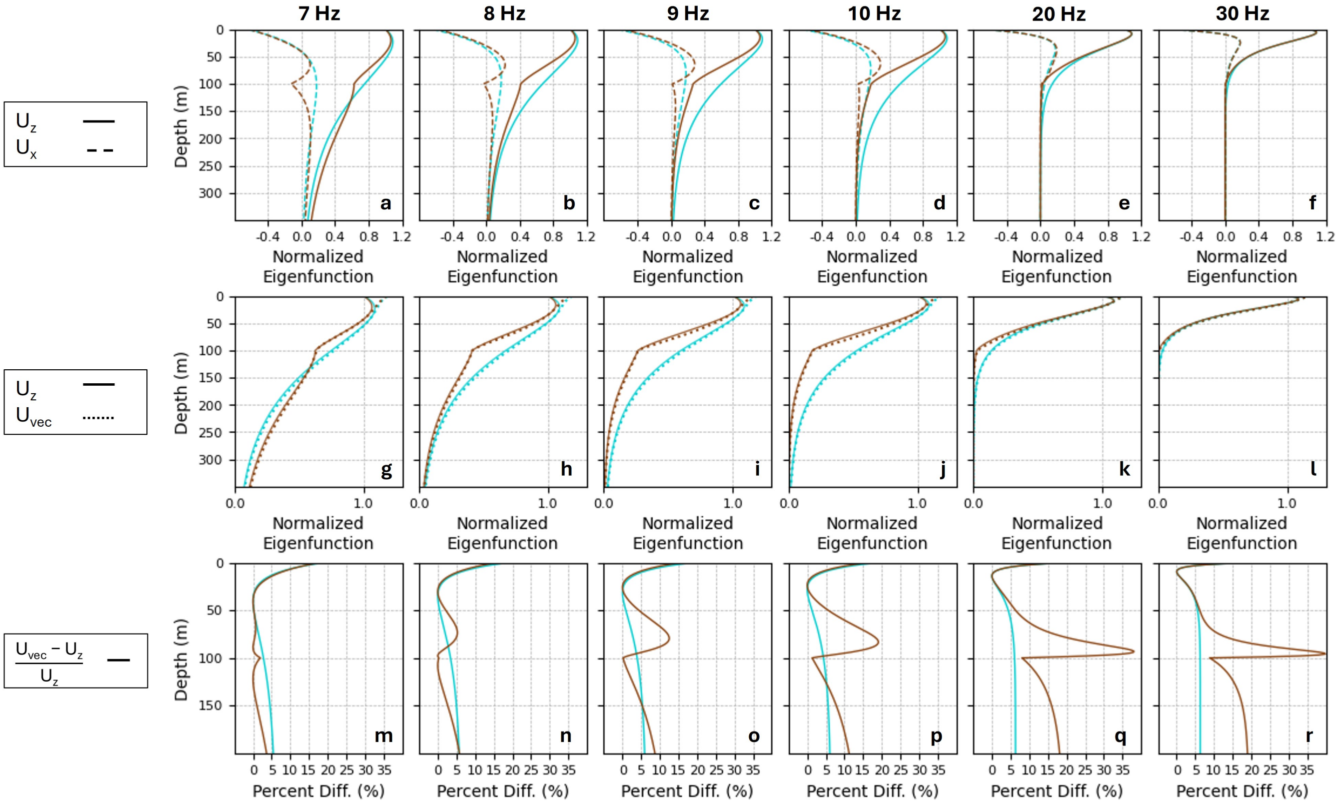

Fig. 7. Description of the depth-sensitivities of the horizontal and vertical Rayleigh-wave displacements for two subsurface models: an infinite-ice layer (blue) and an ice-over-bedrock half-space with the interface at 100 m (brown). (a–f) U_z (solid) and U_x (dashed) eigenfunctions per depth, normalized to $U_z(z = 0) = 1$. (g–k) Comparison of U_z versus the vector displacement U_{vec} (dotted), constructed from U_z and U_x. (m–r) Percent difference between U_{vec} and U_z, highlighting the contributions of U_x. Depths in which the percent differences reach zero correspond to depths where $U_x = 0$ and the elliptical particle motion reverse direction.

Although the U_x amplitudes are smaller than U_z, our goal is to assess how much error may arise in dispersion analysis if vector displacement is ignored and only the vertical component is considered. In Fig. 7g–7l, we compute the vector displacement of the elliptical motion via $U_{\text{vec}} = \sqrt{U_z^2 + U_x^2}$, and compare it to the commonly reported Z-component displacement. The strong contribution of U_x in the shallow region to the vector solution (which decreases with increasing frequency) is evident for both models; that is, the dotted lines show appreciably higher values than solid lines at the shallowest depths. Below this depth, there is a region where the U_x contributions are insignificant before rising again in the infinite-ice model, and displaying even more complex behavior in the ice-bedrock model.

To better visualize this effect and quantify the contribution of the U_x displacement, we calculate the percent difference between U_z and U_{vec}, shown in Fig. 7m–7r. For both models, the near-surface contributions of U_x can reach ∼15% at lower frequencies. In the infinite-ice model, once the depth of particle-motion reversal is crossed, U_x contributions rise again and level off near ∼6%. In the ice-bedrock model, however, the behavior is more complex: after passing the first reversal depth, the strongest U_x contribution appears just above the 100 m interface. This zone becomes narrower but more pronounced with increasing frequency, thus defining a band of intermediate frequencies that would most effectively resolve the changes in horizontal Rayleigh displacement associated with the interface. Below the interface, within the bedrock, the contributions increase toward ∼19%, reflecting the reduced ellipticity associated with propagation in higher-velocity material.

These results point to two main takeaways. At low frequencies, the horizontal component noticeably shapes the vector displacement in the shallow subsurface. At intermediate frequencies, its influence becomes strongest near the interface. In both cases, very high frequencies make these contributions harder to resolve because the displacement changes rapidly over a short depth interval. Together, these observations help explain why the 7.0–20.0 Hz range differs markedly between the Z- and R-component DPs in Fig. 5 and suggest that incorporating both displacement components in dispersion analysis yields a more complete characterization of the subsurface.

The CC-Component

To this point, we have shown that both Z and R components produce DCs that deviate from the numerical true solution, even in this idealized experiment with appropriate data conditioning. Using the depth-sensitivity kernels, we have also illustrated why lower frequencies (around the maximum difference between group and phase velocities) differ between U_z and U_x in response to the shallowest region of the model and the interface depth. We now adopt an approach that exploits the complementary depth sensitivities of the Z and R components, capturing the distinctive low-frequency sensitivity in the R gather while honoring the orthogonality of the Rayleigh motion recorded by each component. To this end, we adopt a complex summation approach to combine the components directly in the shot-gather domain. Importantly, unlike Qiu and others (2019), we treat the R component as imaginary, which helps build intuition for the resulting

DC interpretations. We calculate this combined-complex (CC) component as

$$CC(d,t) = Z(d,t) + iR(d,t)\ . \tag{5}$$

The Fourier transform of a complex-valued signal retains independent positive and negative frequency content, whereas for real-valued signals the negative frequencies are simply mirrored versions of the positive and carry no additional information. Consequently, unlike the real-valued Z and R components used in standard MASW procedures, both frequency branches of the CC-component DP are physically meaningful. In Fig. 8a, we show both the negative and positive frequencies of the DP constructed from the CC gather built from the conditioned Z and R components, which were also used to generate the single-component DPs in Fig. 5c–5d. Comparing the positive-frequency range of the CC DP to the single-component DPs in Fig. 5c–5d, we note that the CC DP exhibits a sharper cutoff at 5 Hz, consistent with the source spectrum used in the modeling, and better facilitates realistic DC picks at these low-frequency limits.

We interpret the differences between the positive and negative frequency branches of the CC DP as reflecting the direction of elliptical particle motion. Where the U_x eigenfunction is positive (Equation (1)), corresponding to overall retrogradational Rayleigh wave motion, the sinusoidal term of U_x is $+90^\circ$ out of phase with the corresponding cosine term of U_z, suggesting that a -90° phase shift of R is required to align the its Rayleigh wave signal with Z. Conversely, at depths where the U_x eigenfunction reverses sign, the resulting negative sinusoid requires a positive phase shift to achieve alignment with U_z. Accordingly, the negative and positive frequency branches of the DP represent negative and positive 90° phase shifts applied to the R component, respectively.

This interpretation potentially explains why, for this ice over bedrock model, the positive-frequency DC exhibits strong amplitude dispersion below approximately 15 Hz, unlike the negative-frequency DC. The progradational motion at depth, expressed on the positive-frequency branch, interacts more strongly with the ice-bedrock interface, whereas the shallower retrograde motion expressed on the negative-frequency branch interacts more weakly with this interface.

In Fig. 8b, we compare the positive-frequency DCs of the conditioned Z and R components with the resulting CC component. The CC component provides a near-exact solution of the numerically modeled DC in the critical sub-15 Hz range, where dispersion related to the ice-bedrock interface is observed. We also plot the average of the conditioned Z and R components, which is similarly accurate but limited to the regions where reasonable picks can be made on the individual Z- and R-component DPs. This represents an important advantage of the CC component, as it extends the low-frequency limit of DC picks — a benefit that is further demonstrated in the field data experiment in Section: Field Example of CC-component Analysis.

Data conditioning is a critical step for accurate dispersion analysis. Although the improvements in the single-component data appear subtle for this idealized experiment, their impact on the resulting CC component is substantial. We illustrate this in Fig. 8b, where the DC picks (in black) are plotted from a CC gather constructed from the raw data used to generate the single-component DPs in Fig. 5a–5b. The comparison between the raw and conditioned CC DC in Fig. 8b underscores that proper data conditioning, aimed at isolating the complete Rayleigh-wave signal from all other energy in the gather domain, is essential for producing an accurate CC component.

In Fig. 8b, we compare the conditioned CC DC with the individual Z- and R-component DCs from both the raw and conditioned panels. The CC-component DC outperforms either single-component DC in the low-frequency range of 8.0–20.0 Hz, which, based on the sensitivity-kernel analysis, is the band that most effectively resolves variations in horizontal Rayleigh-wave displacement associated with the interface. Above $\sim$ 20.0 Hz, the CC component adds little additional information to the interpreted DC.

It is important to compare the CC-component DC with an average of the Z- and R-component DC picks, as implemented previously for exploiting MC datasets (e.g., Calderón-Macías and Simmons, 2008; Picotti and others, 2015). For this idealized synthetic dataset, the differences between the average and CC DCs plotted in Fig. 8b are negligible. However, the average can only be calculated where both Z and R picks exist, whereas constructing a CC-component DP extends the low-frequency resolution beyond what can be picked from the R-component data alone, which limits the frequency range of the average DC. As we will see in the field experiment, the differences between the CC component and the average become more pronounced in sub-optimal surveys and in the presence of noise.

FIELD EXAMPLE OF CC-COMPONENT ANALYSIS

This section evaluates the CC-component dispersion analysis on field data and examines how data-conditioning choices shape the results, given the realities of field surveys with short arrays, sparse receivers, and imperfect data quality.

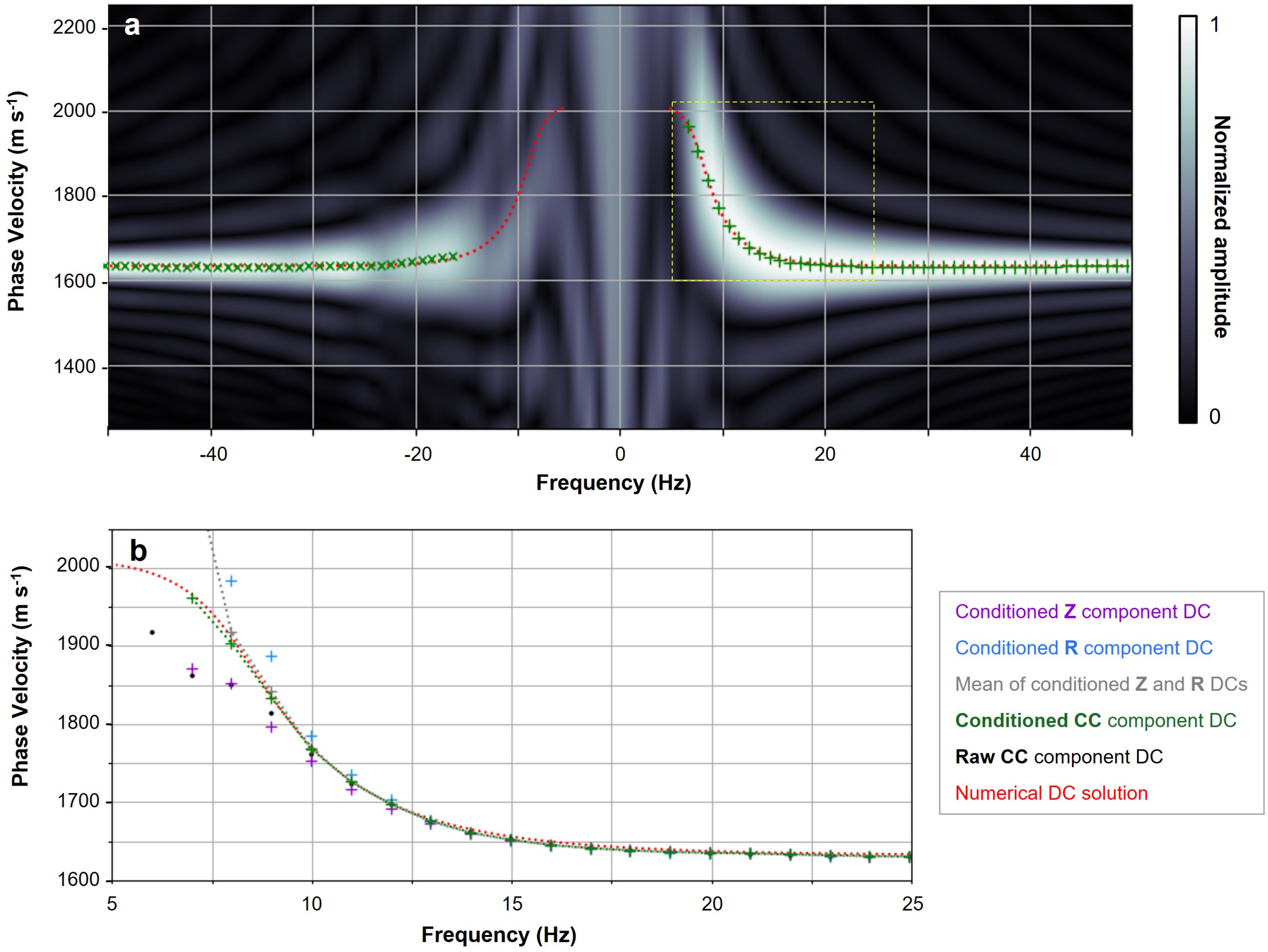

Fig. 8. (a) The DP is generated from the CC gather constructed from the conditioned Z and R datasets (which were used to generate the conditioned DPs in Fig. 5). The associated CC-component DC picks are plotted as green dots against DC picks from a CC gather constructed from raw Z- and R-component data. The numerical solution is shown in red. (b) The raw and conditioned DC picks for Z (purple), R (blue), and CC (green) plotted against the numerical solution as well as the average (gray crosses and dotted line) of the conditioned Z- and R-component DCs. We note that the CC-component DC provides the closest match to the numerical solution across the broadest range of frequencies.

Survey details

In August 2019, Stevens and others (2023) acquired a 2-D active-source seismic survey on the Saskatchewan Glacier (Fig. 9) to complement other geophysical investigations focused on basal ice dynamics (Stevens and others, 2024). The acquisition used nine 3-C geophones (R1 to R9) spaced $\Delta r_x = 10$ m apart forming a linear array of $L = 80$ m aperture oriented along the glacier's centerline. A sledgehammer impacting a metal plate served as a seismic energy source at 25 station locations (S01 to S25) distributed over a 240 m span centered on the array with a maximum two-sided offset of $d_{max} = 160$ m. A tenth 3-C geophone was moved to every source station to record the excitation time of each shot.

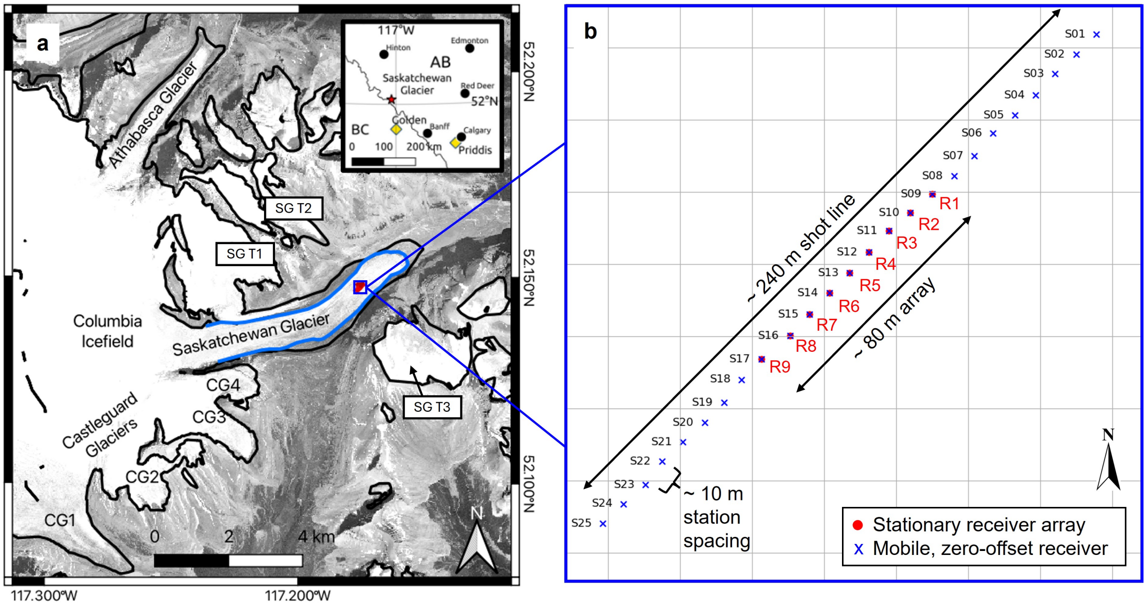

Fig. 9. (a) Map reproduced from Stevens and others (2023) showing the location of the Saskatchewan Glacier in the Canadian Rocky Mountains, Canada (see inset map). Basemap imagery: Orthorectified 4-band PlanetScope scene accessed via Planet.com. CG# = Castleguard Glacier Number #; SG T# = Saskatchewan Glacier (former) Tributary glacier # (b) Geometry of the active-source seismic experiment conducted in the ablation zone involving a stationary array of nine 3-C geophones (R1-R9) linearly spaced at 10 m to form an array of aperture $L = 80$ m. Source station locations S01-S25, also spaced 10 m apart, are shown as blue Xs.

Data conditioning

Fig. 10 shows examples of raw Z- and R-component shot gathers for station S02, which exhibit a similar phase relationship between the Z and R components as observed in the synthetic experiments. We note the presence of a noisy zero-offset trace and the absence of traces at receivers R2 and R9. These data issues reflect the inherent challenges in field experiments arising due to equipment malfunction rather than indicative of underlying wavefield behavior.

As Foti and others (2018) emphasize, careful data conditioning prevents DPs from appearing noisier or more complex than the subsurface structure warrants. In Supplementary Material Text S3, we highlight an aspect that prior studies have rarely examined: how conditioning steps influence the R-component DPs

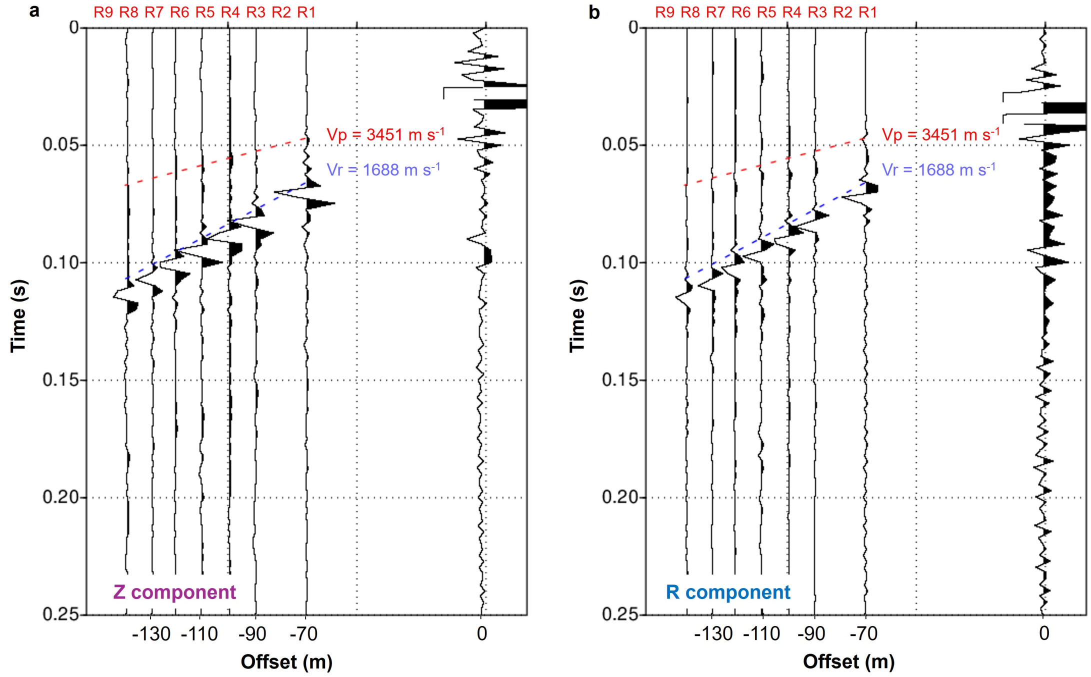

Fig. 10. Raw (a) Z- and (b) R-component shot-gather data for station S02. The zero-offset trace recorded by the mobile geophone is used to window the continuously recorded data on geophones R1-R9 into shot gathers. V_p and V_r moveout velocities calculated by Stevens and others (2023) are plotted. Note the missing traces at R2 and R9. Additionally, direct P-wave arrival is weaker on the Z- versus the R-component data because of the predominantly horizontal particle motion. Strong Rayleigh wave energy is recorded on both components.

relative to that of the Z component. Using the shot at S02 from the Saskatchewan Glacier dataset, we show that most processing steps affect both components in broadly comparable ways. These steps remove noisy near-offset traces, window the gathers to capture the full Rayleigh-wave signal across offsets, and interpolate missing traces rather than leaving them empty or null. One procedure, however, provides a clearer benefit to the R-component DP — muting the direct-wave energy. Because the radial component records stronger direct-wave energy, applying this mute produces stronger and more consistent low-frequency amplitudes in the R-component DP (compare Fig. S3.4 to Fig. S3.5). Overall, the conditioning workflow stabilizes the DPs and modestly strengthens their amplitudes, but the resulting DC picks for both Z and R components change only slightly in this limited-offset, noisy field dataset.

In Fig. 11, we compare the positive-frequency CC-component DPs generated at different stages of processing for shot at S02 and overlay the associated DC picks, along with the single-component picks from equivalently processed Z and R gathers. The CC component stays stable across the full workflow and yields much steadier DC curves than either single component, particularly at frequencies below 40 Hz.

Muting the direct wave exerts a smaller influence on the CC-component DPs and DCs than we observed in the synthetic experiment, likely due to the noise level in the field data. For field applications, interpolating missing traces plays a more important role than muting: leaving gaps as empty or null traces introduces beat-like distortions in the DPs (compare single-component DPs in Fig. S3.4 and S3.5 and CC-component DPs in Fig. 11a versus 11b).

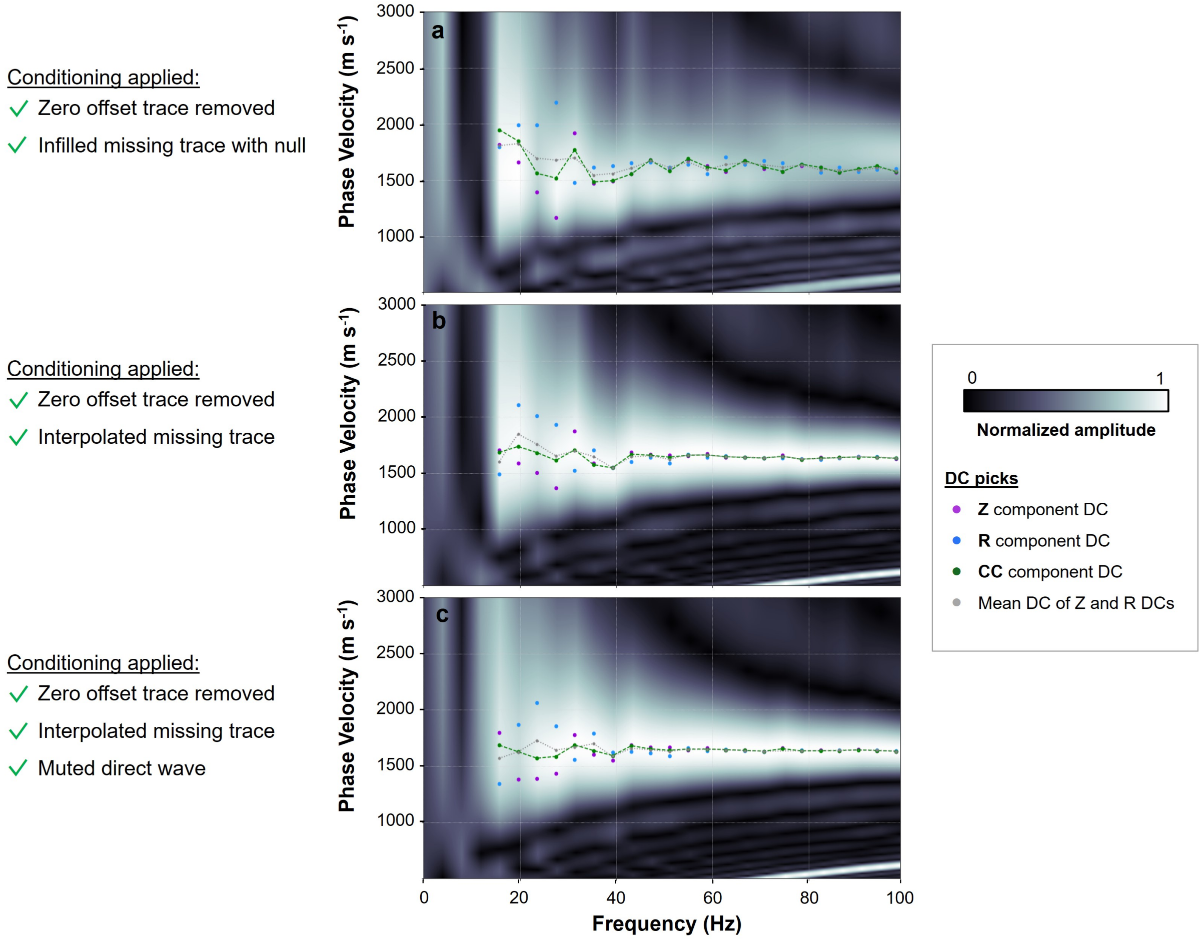

Fig. 11. Comparison of CC-component DPs generated at different stages of processing for shot at S02 and overlaid with the associated DC picks, along with the single-component picks from equivalently processed Z- and R-component gathers. (a) Zero offset trace is removed and missing offset is infilled with null trace (b) Zero offset trace is removed and missing offset is interpolated (c) Zero offset trace is removed, missing offset trace is interpolated and direct wave is muted.

Supergather processing

Interpolating traces at certain offsets however can be a messy task with subjective decisions, and such infilling of missing traces can be more easily achieved with better representation of the physical environment via supergather processing (Hesthammer and Løkkebø, 1997).

Stacking is a well-established seismic processing step used to improve signal-to-noise ratio (SNR) and can be applied in many data dimensions. In the time-offset domain, stacking multiple shots that share common offsets is commonly referred to as building a supergather. The earliest documented reference to this approach is Hesthammer and Løkkebø (1997). To build a supergather from several shots, each gather is first windowed to align traces of the same offsets by applying time-shifts as necessary to each shot gather. The time-shifted gathers are stacked by averaging traces at similar offsets.

Supergather processing is typically applied over a fixed aperture to improve DP SNR, and Vantassel and Cox (2022) provides an excellent comparison of this method (referred to as time-domain stacking) with other approaches for improving DP SNR within a fixed aperture. A common drawback across many of these methods (including supergather processing) is that, in areas characterized by lateral heterogeneity or structural complexity spatial averaging can obscure subtle subsurface features and reduce the accuracy of derived models. That said, as discussed earlier in Section: V_s-modeling using Surface Rayleigh Waves, the MASW-derived velocity profile inherently represent an average over the maximum source–receiver offset, meaning that trace mixing introduced by supergathers is often secondary to the choice of maximum offset itself.

In this study, we implement a simple variation of conventional supergather processing in which offsets are retained even where input gather offsets do not overlap. The mechanics of this process are illustrated in Fig. 12. This approach provides two complementary benefits: it infills missing offsets without requiring interpolation and also improves dispersion analysis by effectively increasing the data aperture. Extending the data aperture enhances the resolution of low-frequency content in the DPs and extends the depth of investigation. This relationship between array length and dispersion resolution is well demonstrated for Z-component data by Socco and Strobbia (2004) and Foti and others (2018). In Supplementary Material Text S4 we discuss how the array aperture similarly impacts the CC-component DP.

In Fig. 13, we show the DPs constructed from the Z, R, and CC components for each of the four experiments, which differ in the individual shots and shot density used to generate the supergather. The first and second experiments (Fig. 13a–13c and 13d–13f, respectively) compare the DPs from two single

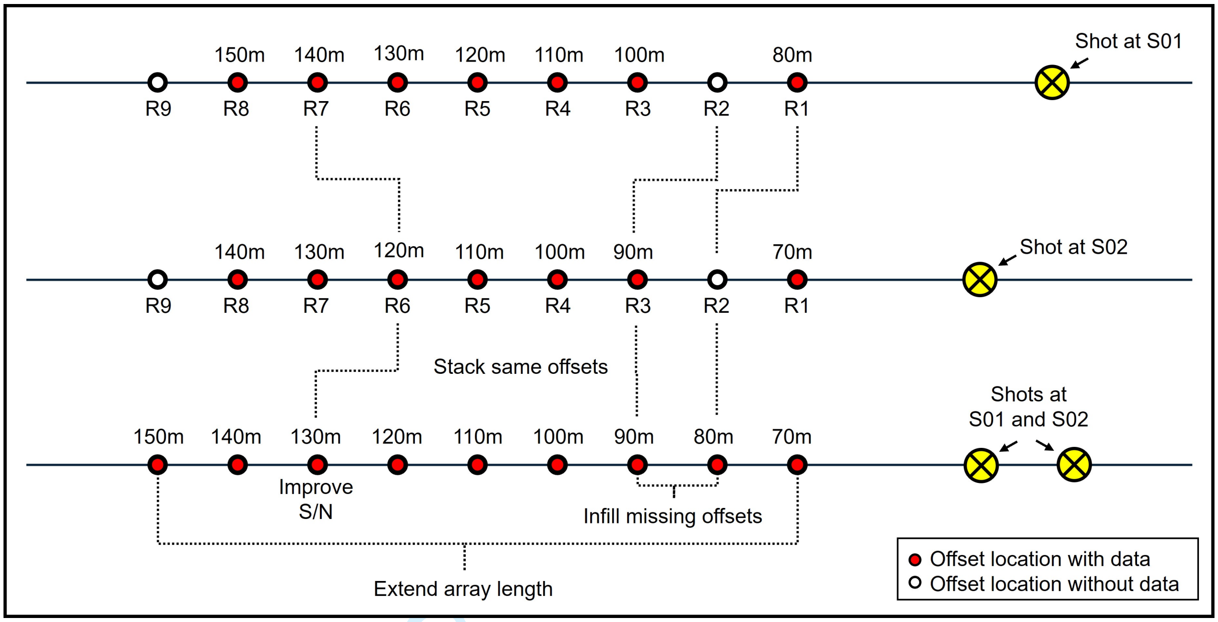

Fig. 12. Description of the offset coverage and array length for shots #1, #2, and a supergather generated from both #1 and #2.

shot gathers at locations S01 and S02. The third experiment (Fig. 13g–13i) is a low-fold supergather built from these two individual shots but trimmed to match the 70 m aperture (80 – 150 m offset) of the single-shot experiments. The fourth experiment is a high-fold supergather composed of shot locations S01 through S08 and with a 140 m aperture (10 – 150 m offset).

Although the DPs are plotted up to 100 Hz, estimates of the recoverable wavelengths are constrained by the Nyquist sampling theorem (Socco and Strobbia, 2004; de Lucena and Taioli, 2014); these bounds ideally should guide the selection of DC picks. In the Saskatchewan Glacier experiment, where the receiver spacing is 10 m, the shortest resolvable wavelength is 20 m. In noisy field data, the Nyquist-based estimate of the longest recoverable wavelength may be optimistic. For arrays with 70 m aperture (in the first through third experiments) and 140 m (high-fold supergather experiment), the corresponding longest recoverable wavelengths are approximately 140 m and 280 m, respectively. Under noisy conditions, a more conservative approach involves sampling at twice the Nyquist rate, meaning that wavelengths equal in length to the array are well sampled and can be recovered with high confidence.

In Fig. 13, automatic picks of the high-amplitude DC trend generated by the internal *MASWaves* algorithm are shown as colored dots. Ideally, the subset of picks within the expected lower and upper wavelength limits of the experiment would be used as input for inversion. However, for both the Z and R components in DPs derived from a single-shot-gather (Fig. 13a–13b for Z and R components of shot S1, respectively, and Fig. 13d–13e for Z and R components of shot S2, respectively) and in a DPs for low-fold supergather experiments (Fig. 13g–13h for Z and R components, respectively), significant noise reduces confidence in the lower-frequency picks. Consequently, subjective adjustment of the picks is required for the single-component modes; the reliable DC picks are indicated as colored crosses. This truncation of low-frequency picks ultimately limits depth sensitivity, which is undesirable. By contrast, such adjustments were unnecessary for the corresponding CC-component experiments, allowing reliable DC picks up to the conservative upper wavelength limit.

With a high-fold supergather (SG1–8) comprising shot locations S01 through S08 (Fig. 13j–13l), the SNR of the DPs improved noticeably across all components. All picks between the minimum and maximum resolvable wavelengths were retained, although an argument could be made for removing some of the low-frequency noisy picks still observed in the R-component experiment (Fig. 13k). The convergence between the Z and CC picks results under high fold suggests that, with sufficient stacking, the relative advantage of the CC component may diminish. Nonetheless, the CC component continues to exhibit a lower misfit, highlighting its robustness. Overall, all four experiments highlight the comparative resilience of the CC processing enabled by 3-C data collection and its lower sensitivity to noise that typically affects the Z and R components.

In Fig. 14, we overlay the DC picks for the Z, R, and CC components for both supergather experiments, along with the average of the Z- and R-component DCs for comparison. For the low-fold experiment (Fig. 14a), the CC component clearly provides the extended low-frequency picks that cannot be reasonably identified on the Z or R components and therefore cannot be represented in their average. In the high-fold experiment (Fig. 14b), the average extends to lower frequencies because the range of resolvable Z and R DC picks improves with fold. Even so, the variability in the CC-component picks remains noticeably lower than in the average, consistent with the expectation that, for the resolvable band above roughly 15 Hz, the curve should be fairly flat.

This expectation is based on the results of Stevens and others (2023), which point toward a bedrock depth on the order of 150–200 m—conditions that, according to our sensitivity-kernel analysis, require frequencies below roughly 15 Hz to resolve. Recall from the kernels in Fig. 5e, f5k, and f5q that at 20 Hz, the sensitivities of the ice-bedrock model with a 100 m interface and of an infinitely homogeneous ice layer are nearly identical. This indicates that at and above this frequency, it becomes challenging to distinguish between the two models, as the Rayleigh-wave velocity effectively reflects the shallow ice alone. For the

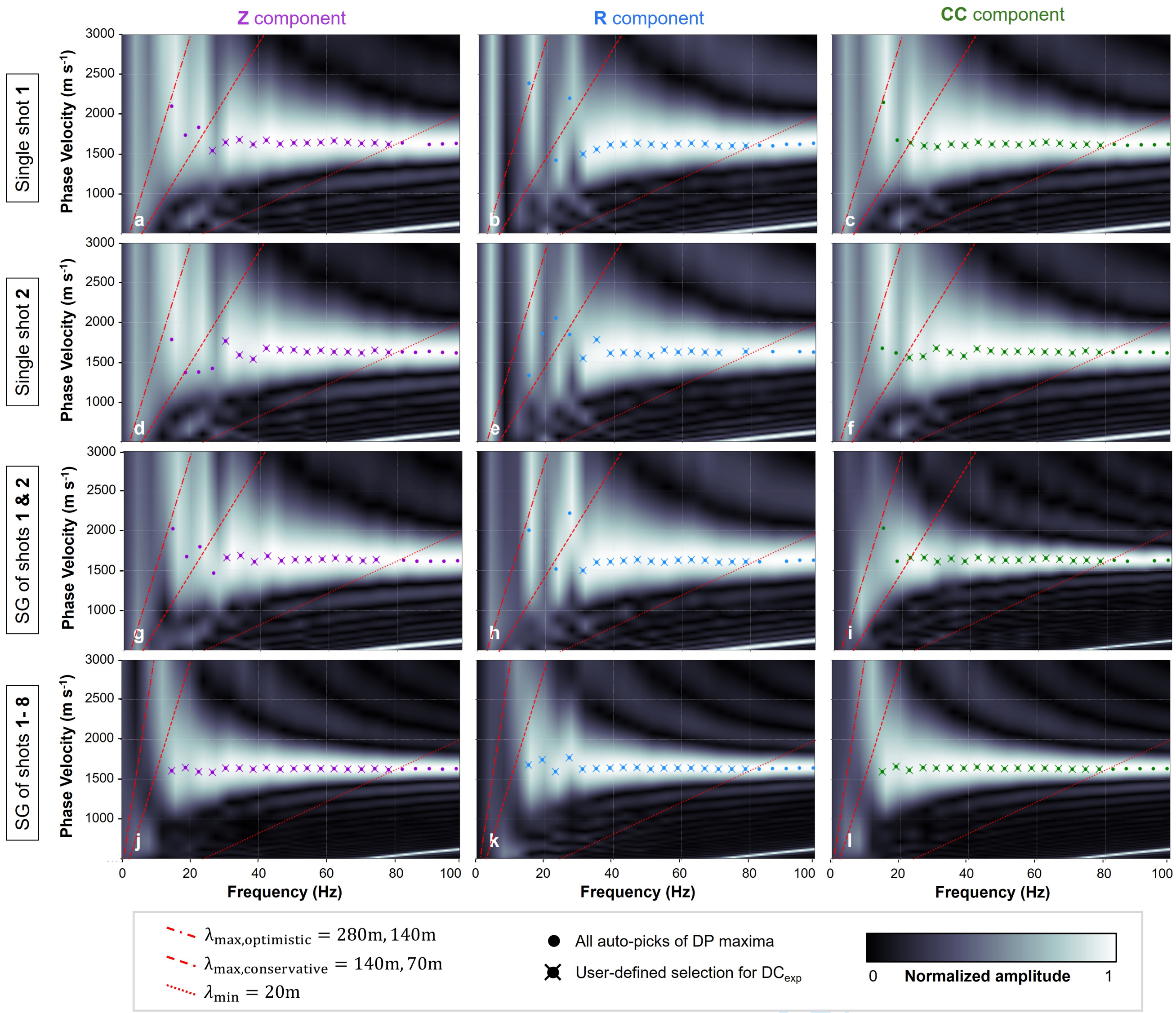

Fig. 13. DPs for Z-, R- and CC-components for four experiments: (a–c) shot gather at location S01; (d–e) shot gather at location S02; (g–i) supergather of shots at locations S01 and S02; and (j–l) supergather of shots at locations S01 through S08. All auto-picks selected by the internal *MASWaves* algorithm are plotted as dots; however only a few of these picks (crosses) represent the higher confidence DC picks between the expected lower and conservative upper wavelength limits of the experiment based on survey design. In some cases, manual de-selection of noisy picks on the Z and R components between these limits was necessary at low frequencies.

deeper bedrock likely present at Saskatchewan, this transition frequency shifts even lower.

Nonetheless, we can still estimate the shallow-ice structure. Averaging the picks on the high-fold CC-component super-gather yields a mean $V_r = 1645 \pm 15$ m s^{-1}, 45 m s^{-1} slower than the linear-moveout V_r of 1690 m s^{-1} reported by Stevens and others (2023). This difference likely reflects the inherent subjectivity

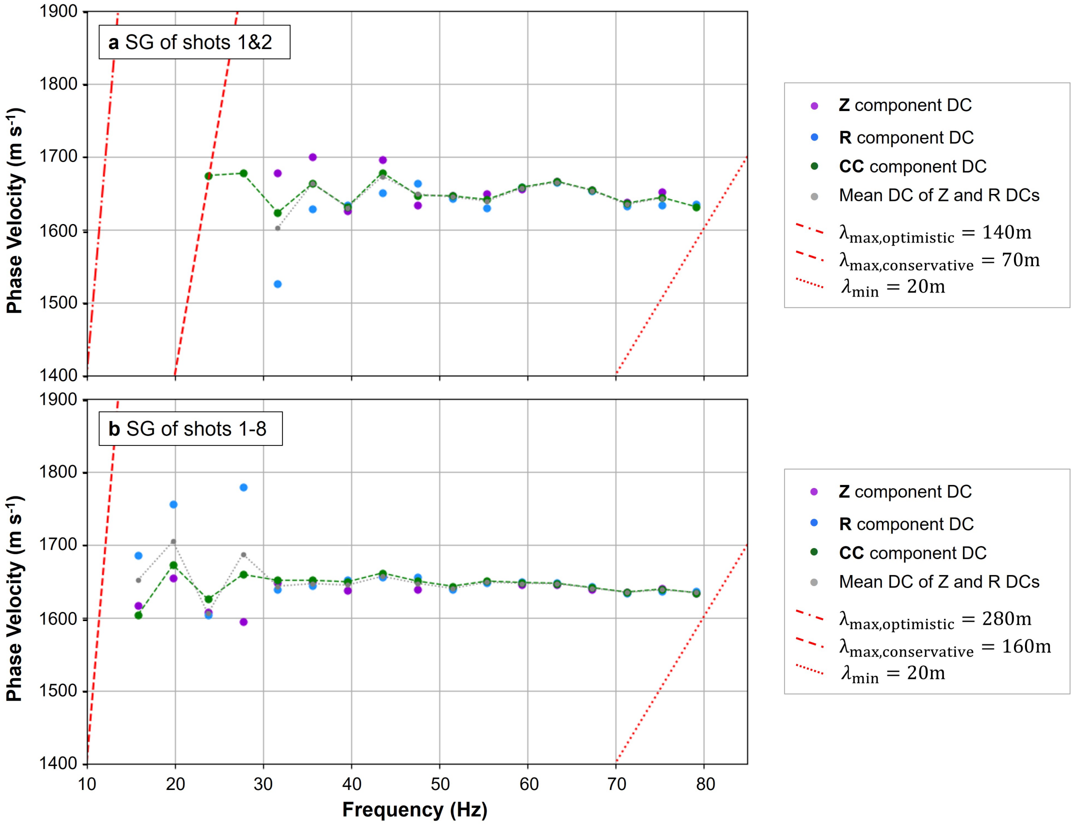

Fig. 14. Comparing the Z, R, and CC dispersion curves from (a) the supergather built from shots S01–S02 and (b) the supergather built from shots S01–S08. For each case, we also include the average of the Z and R curves. Similar to the single-shot investigation in Fig. 11, the CC component continues to yield a smoother, more stable curve than the average and, importantly, captures the low-frequency picks that the individual components struggle to recover.

in picking linear moveouts, whereas the dispersion-based analysis is less subjective, particularly when using the CC component to improve SNR.

DISCUSSION

The Z- and R-component data acquire orthogonal particle motions of Rayleigh waves. We have demonstrated that by leveraging both, the complete elliptical particle motion can be reconstructed via a complex-summation and the resulting CC-component produces a more accurate representation of true dispersion and additionally benefits SNR in field data. The improved accuracy stems from the complementary sensitivity of the R-component to subsurface layering, providing information about layered media that is not fully captured by Z-component data alone.

In glacial settings, where englacial stratification may be subtle and SNR is often degraded by challenging field conditions, DC quality and fidelity can propagate into substantial uncertainty in inverted $V_s(z)$ structure. The improvements of the CC-component DCs therefore translates directly into tighter constraints on inverted V_s structure, which governs estimates of ice thickness, basal conditions, and englacial heterogeneity.

Realizing this benefit, however, requires inversion strategies capable of honoring the subtle yet meaningful differences introduced by the CC-component. A natural progression of this work is therefore to evaluate inverted solutions across diverse field datasets using a sufficiently flexible inversion framework. Testing of a trans-dimensional Bayesian inversion strategy for such datasets is currently ongoing.

Practical Considerations for Multi-Component Acquisition

Throughout this manuscript, we outline practical data-conditioning considerations for implementing the CC-component approach, including interpolation through supergather construction and muting near-offset traces where direct-wave energy strongly influences the R-component (Supplementary Text S3). Here, we briefly discuss acquisition strategies that emerge from these findings.

Firstly, because near offsets are removed in this workflow, practitioners can strategically increase receiver spacing without sacrificing usable information. Our synthetic analysis in Supplementary Text S4 demonstrates that prioritizing array aperture over dense receiver spacing is judicious for Rayleigh-wave dispersion analysis, improving depth of investigation without compromising low-frequency dispersion resolution. To further optimize offset coverage, shots can be placed between receiver locations, ideally at half the receiver spacing, since standard dispersion panel construction assumes equal source–receiver offsets.

A final consideration for multi-component acquisition is the uniform orientation of the receivers. Horizontal components should be aligned consistently, either with one arm inline with the source-line and the other oriented consistently clockwise or counter-clockwise, or more simply along cardinal directions such as North and East. Consistent orientation is important for facilitating the radial–transverse rotation. In addition, careful sensor leveling can minimize cross-component contamination and ensure that the reconstructed elliptical particle motions accurately reflect subsurface structure.

CONCLUSIONS

We present a novel framework for leveraging 3-C seismic data in glacial environments through the complex-summation approach, which treats the Z- and R-components as the real and imaginary parts, respectively. We demonstrate that the resulting CC-component DC provides a more accurate representation of true dispersion and, by naturally enhancing low-frequency amplitudes in the DP, extends the depth of investigation compared with a traditional Z-component-only analysis. Even under field-limited conditions, the improved accuracy and confidence of CC-component DC picks can strengthen constraints on glacier geometry and elastic properties derived from subsequent $V_s(z)$ inversions.

A central aim of this work is to make the mechanics of Rayleigh-wave dispersion analysis both accessible and practical, enabling the CC-component MC-MASW approach to be understood and applied intuitively. In doing so, the study provides a tutorial-like framework for 3-C seismic analysis in glacial environments, revisiting the necessary theory for both vertical and horizontal components at each stage —building on previous literature that has largely focused on vertical data. Beyond methodological insights for MC-MASW, our results thus also provide field-ready strategies to maximize the value of glacial MASW surveys.

DATA AVAILABILITY

Synthetic glacial datasets and models are available on GitHub (https://github.com/samara-melody/MC-MASW), alongside relevant processing scripts. We refer the reader to Stevens and others (2023) and their accompanied supplemental material for information regarding accessibility of the Saskatchewan Glacier field datasets.

ACKNOWLEDGMENTS

The Mines Geophysics Department, Mines Glaciology Laboratory, and the Center for Wave Phenomena each supported the author's research through scholarship. The author gives special thanks to H. Verboncoeur and N. Punithan for insightful discussions and shared domain knowledge.

Analyses in this work were conducted using a range of open-source software packages. We acknowledge the efforts of the developers and contributors who advance accessible tools for scientific research. We used the software *MASWaves* (Olafsdottir and others, 2018) for dispersion curve forward modeling and analysis and *disba* for numerical modeling. We carried out seismic data processing using *ObsPy* (Beyreuther and

others, 2010) for field data in MiniSEED format and *Seismic Unix* for SEGY-formatted data (Stockwell Jr, 1999). Additional numerical and symbolic computations, as well as data visualization, were supported by Python libraries including *NumPy* (Harris and others, 2020), *SymPy* (Meurer and others, 2017), *pandas* (McKinney, 2010) and *Matplotlib* (Hunter, 2007).

REFERENCES

Abdialim S, Hakimov F, Kim J, Ku T and Moon SW (2021) Seismic site classification from HVSR data using the Rayleigh wave ellipticity inversion: A case study in Singapore. *Earthquakes and Structures*, **21**(3), 231–8

Agnew RS, Clark RA, Booth AD, Brisbourne AM and Smith AM (2023) Measuring seismic attenuation in polar firn: method and application to Korff Ice Rise, West Antarctica. *Journal of Glaciology*, **69**(278), 2075–2086 (doi: 10.1017/jog.2023.82)

Aki K and Richards PG (2002) *Quantitative Seismology*. University Science Books, ISBN 0935702962

Ammon CJ, Velasco AA, Lay T and Wallace TC (2020) *Foundations of Modern Global Seismology*. Academic Press, ISBN 0128156791

Aster RC and Winberry JP (2017) Glacial seismology. *Reports on Progress in Physics*, **80**(12), 126801 (doi: 10.1088/1361-6633/aa8473)

Bennett MR (2022) *Our Dynamic Earth: A Primer*. Springer International Publishing, Cham, ISBN 3030903532 (doi: 10.1007/978-3-030-90351-0_9)

Beyreuther M, Barsch R, Krischer L, Megies T, Behr Y and Wassermann J (2010) ObsPy: A Python toolbox for seismology. *Seismological Research Letters*, **81**(3), 530–533

Bignardi S, Mantovani A and Zeid NA (2016) OpenHVSR: imaging the subsurface 2D/3D elastic properties through multiple HVSR modeling and inversion. *Computers & Geosciences*, **93**, 103–113

Boaga J, Cassiani G, Strobbia CL and Vignoli G (2013) Mode misidentification in Rayleigh waves: Ellipticity as a cause and a cure. *Geophysics*, **78**(4), EN17–EN28

Bohlen T, De Nil D, Köhn D and Jetschny S (2016) SOFI2D seismic modeling with finite differences: 2D—elastic and viscoelastic version. *user guide*, accessed: 2024-03-01

Calderón-Macías C and Simmons J (2008) *Constrained surface wave inversion from 9-component seismic reflection data*, 1063–1067. Society of Exploration Geophysicists (doi: 10.1190/1.3059109)

Church G, Bauder A, Grab M, Rabenstein L, Singh S and Maurer H (2019) Detecting and characterising an englacial conduit network within a temperate Swiss glacier using active seismic, ground penetrating radar and borehole analysis. *Annals of Glaciology*, **60**(79), 193–205 (doi: 10.1017/aog.2019.19)

Crice D (2005) MASW, the wave of the future editorial. *Journal of Environmental & Engineering Geophysics*, **10**(2), 77–79 (doi: 10.2113/JEEG10.2.77)

Dal Moro G, Moura R and Moustafa S (2015) Multi-component joint analysis of surface waves. *Journal of Applied Geophysics*, **119**, 128–138

Dal Moro G, Al-Arifi N and Moustafa S (2017) Analysis of Rayleigh-wave particle motion from active seismics. *Bulletin of the Seismological Society of America*, **107**(1), 51–62

de Lucena RF and Taioli F (2014) Rayleigh wave modeling: A study of dispersion curve sensitivity and methodology for calculating an initial model to be included in an inversion algorithm. *Journal of Applied Geophysics*, **108**, 140–151 (doi: 10.1016/j.jappgeo.2014.07.007)

Diez A and Eisen O (2015) Seismic wave propagation in anisotropic ice–Part 1: Elasticity tensor and derived quantities from ice-core properties. *The Cryosphere*, **9**(1), 367–384

Faria SH, Weikusat I and Azuma N (2014) The microstructure of polar ice. part ii: State of the art. *Journal of Structural Geology*, **61**, 21–49

Foti S, Hollender F, Garofalo F, Albarello D, Asten M, Bard PY, Comina C, Cornou C, Cox B, Di Giulio G and others (2018) Guidelines for the good practice of surface wave analysis: a product of the InterPACIFIC project. *Bulletin of Earthquake Engineering*, **16**, 2367–2420 (doi: 10.1007/s10518-017-0206-7)

Gaiser J (1999) Applications for vector coordinate systems of 3-D converted-wave data. *The Leading Edge*, **18**(11), 1290–1300

Glazer M, Dobiński W, Marciniak A, Majdański M and Błaszczyk M (2020) Spatial distribution and controls of permafrost development in non-glacial Arctic catchment over the Holocene, Fuglebekken, SW Spitsbergen. *Geomorphology*, **358**, 107128

Harris CR, Millman KJ, der Walt SJ, Gommers R, Virtanen P, Cournapeau D, Wieser E, Taylor J, Berg S, Smith NJ, Kern R, Picus M, Hoyer S, van Kerkwijk MH, Brett M, Haldane A, del Río JF, Wiebe M, Peterson P, Gérard-Marchant P, Sheppard K, Reddy T, Weckesser W, Abbasi H, Gohlke C and Oliphant TE (2020) Array programming with NumPy. *Nature*, **585**(7825), 357–362 (doi: 10.1038/s41586-020-2649-2)

Hesthammer J and Løkkebø SM (1997) Combining seismic surveys to improve data quality. *First Break*, **15**(4)

Hunter JD (2007) Matplotlib: A 2D graphics environment. *Computing in Science & Engineering*, **9**(3), 90–95 (doi: 10.1109/MCSE.2007.55)

Ibs-von Seht M and Wohlenberg J (1999) Microtremor measurements used to map thickness of soft sediments. *Bulletin of the Seismological Society of America*, **89**(1), 250–259 (doi: 10.1785/BSSA0890010250)

Ikeda T, Matsuoka T, Tsuji T and Nakayama T (2015) Characteristics of the horizontal component of Rayleigh waves in multimode analysis of surface waves. *Geophysics*, **80**(1), EN1–EN11

Ivanov J, Tsoflias G, Miller RD, Peterie S, Morton S and Xia J (2016) Impact of density information on Rayleigh surface wave inversion results. *Journal of Applied Geophysics*, **135**, 43–54, ISSN 0926-9851 (doi: https://doi.org/10.1016/j.jappgeo.2016.09.011), new trends in Induced Polarization

Johansen TA, Ruud B, Bakke NE, Riste P, Johannessen EP and Henningsen T (2011) Seismic profiling on Arctic glaciers. *First Break*, **29**(2) (doi: 10.3997/1365-2397.20112st1)

Killingbeck S, Livermore P, Booth A and West L (2018) Multimodal layered transdimensional inversion of seismic dispersion curves with depth constraints. *Geochemistry, Geophysics, Geosystems*, **19**(12), 4957–4971 (doi: 10.1029/2018GC008000)

Killingbeck S, Schmerr N, Montgomery L, Booth A, Livermore P, Guandique J, Miller OL, Burdick S, Forster R, Koenig L and others (2020) Integrated borehole, radar, and seismic velocity analysis reveals dynamic spatial variations within a firn aquifer in southeast Greenland. *Geophysical Research Letters*, **47**(18), e2020GL089335 (doi: 10.1029/2020GL089335)

Koller M, Chatelain J, Guillier B, Duval A, Atakan K, Lacave C, Bard P and participants S (2004) Practical user guideline and software for the implementation of the H/V ratio technique on ambient vibrations: measuring conditions, processing method and results interpretation. In *13th World Conference on Earthquake Engineering*

Kuehn T, Holt JW, Johnson R and Meng T (2024) Active seismic refraction, reflection, and surface-wave surveys in thick debris-covered glacial environments. *Journal of Geophysical Research: Earth Surface*, **129**(1), e2023JF007304 (doi: 10.1029/2023JF007304)

Lawrence JF, Wiens DA, Nyblade AA, Anandakrishnan S, Shore PJ and Voigt D (2006) Rayleigh wave phase velocity analysis of the Ross Sea, Transantarctic Mountains, and East Antarctica from a temporary seismograph array. *Journal of Geophysical Research: Solid Earth*, **111**(B6) (doi: 10.1029/2005JB003812)

Lay T and Wallace TC (1995) *Modern Global Seismology*. Elsevier, ISBN 012732870X

Liner C (2012) *Elements of seismic dispersion: A somewhat practical guide to frequency-dependent phenomena*. Society of Exploration Geophysicists, ISBN 156080291X

McKinney W (2010) Data structures for statistical computing in Python. In *Proceedings of the 9th Python in Science Conference*, 51–56

Meurer A, Smith CP, Paprocki M, Čertík O, Kirpichev SB, Rocklin M, Kumar A, Ivanov S, Moore JK, Singh S, Rathnayake T, Vig S, Granger BE, Muller RP, Bonazzi F, Gupta H, Vats S, Johansson F, Pedregosa F, Curry MJ, Terrel AR, Roučka v, Saboo A, Fernando I, Kulal S, Cimrman R and Scopatz A (2017) SymPy: symbolic computing in Python. *PeerJ Computer Science*, **3**, e103, ISSN 2376-5992 (doi: 10.7717/peerj-cs.103)

Mi B, Hu Y, Xia J and Socco LV (2019) Estimation of horizontal-to-vertical spectral ratios (ellipticity) of Rayleigh waves from multistation active-seismic records. *Geophysics*, **84**(6), EN81–EN92, ISSN 0016-8033 (doi: 10.1190/geo2018-0651.1)

Millan R, Mouginot J, Rabatel A and Morlighem M (2022) Ice velocity and thickness of the world's glaciers. *Nature Geoscience*, **15**(2), 124–129

Olafsdottir EA, Erlingsson S and Bessason B (2018) Open software for analysis of MASW data. In *Proceedings of the 16th European Conference on Earthquake Engineering*, accessed: 2024-05-01

Pan Y, Schaneng S, Steinweg T and Bohlen T (2018) Estimating S-wave velocities from 3D 9-component shallow seismic data using local Rayleigh-wave dispersion curves–A field study. *Journal of Applied Geophysics*, **159**, 532–539

Papadopoulou M (2021) *Surface-wave methods for mineral exploration*. Ph.D. thesis, Politecnico di Torino

Park CB, Miller RD and Xia J (1998) Imaging dispersion curves of surface waves on multi-channel record. In *SEG technical program expanded abstracts 1998*, 1377–1380, Society of Exploration Geophysicists (doi: 10.1190/1.1820161)

Park CB, Miller RD and Xia J (1999) Multichannel analysis of surface waves. *Geophysics*, **64**(3), 800–808 (doi: 10.1190/1.1444590)

Picotti S, Vuan A, Carcione JM, Horgan HJ and Anandakrishnan S (2015) Anisotropy and crystalline fabric of Whillans Ice Stream (West Antarctica) inferred from multicomponent seismic data. *Journal of Geophysical Research: Solid Earth*, **120**(6), 4237–4262 (doi: https://doi.org/10.1002/2014JB011591)

Picotti S, Francese R, Giorgi M, Pettenati F and Carcione JM (2017) Estimation of glacier thicknesses and basal properties using the horizontal-to-vertical component spectral ratio (HVSR) technique from passive seismic data. *Journal of Glaciology*, **63**(238), 229–248 (doi: 10.1017/jog.2016.135)

Podolskiy EA and Walter F (2016) Cryoseismology. *Reviews of Geophysics*, **54**(4), 708–758 (doi: 10.1002/2016RG000526)

Preiswerk LE, Michel C, Walter F and Fäh D (2019) Effects of geometry on the seismic wavefield of alpine glaciers. *Annals of Glaciology*, **60**(79), 112–124 (doi: 10.1017/aog.2018.27)

Qin L, Qiu H, Nakata N, Booth A, Zhang Z, Karplus M, McKeague J, Clark R and Kaip G (2024) High-resolution characterization of the firn layer near the West Antarctic ice sheet divide camp with active and passive seismic data. *Geophysical Research Letters*, **51**(12), e2024GL108933

Qiu X, Wang Y and Wang C (2019) Rayleigh-wave dispersion analysis using complex-vector seismic data. *Near Surface Geophysics*, **17**(5), 487–499

Redpath BB (1973) Seismic refraction exploration for engineering site investigations. Technical report, Army Engineer Waterways Experiment Station (doi: 10.2172/4409605)

Richart FE, Hall JR and Woods RD (1970) *Vibrations of soils and foundations*. Prentice-Hall

Smith AM (1997) Variations in basal conditions on Rutford Ice Stream, West Antarctica. *Journal of Glaciology*, **43**(144), 245–255 (doi: 10.3189/S0022143000003191)

Socco L and Strobbia C (2004) Surface-wave method for near-surface characterization: A tutorial. *Near Surface Geophysics*, **2**(4), 165–185 (doi: 10.3997/1873-0604.2004015)

Stevens NT, Roland CJ, Zoet LK, Alley RB, Hansen DD and Schwans E (2023) Multi-decadal basal slip enhancement at Saskatchewan glacier, Canadian Rocky Mountains. *Journal of Glaciology*, **69**(273), 71–86 (doi: 10.1017/jog.2022.45)

Stevens NT, Zoet LK, Hansen DD, Alley RB, Roland CJ, Schwans E and Shepherd CS (2024) Icequake insights on transient glacier slip mechanics near channelized subglacial drainage. *Earth and Planetary Science Letters*, **627**, 118513 (doi: 10.1016/j.epsl.2023.118513)

Stockwell Jr JW (1999) The CWP/SU: Seismic Unix package. *Computers & Geosciences*, **25**(4), 415–419

Sun L, Wang Y and Qiu X (2022) Rayleigh-wave dispersion analysis and inversion based on the rotation. *Sensors*, **22**(3), 983

Tourei A, Ji X, Rocha dos Santos G, Czarny R, Rybakov S, Wang Z, Hallissey M, Martin ER, Xiao M, Zhu T, Nicolsky D and Jensen A (2024) Mapping Permafrost Variability and Degradation Using Seismic Surface Waves, Electrical Resistivity, and Temperature Sensing: A Case Study in Arctic Alaska. *Journal of Geophysical Research: Earth Surface*, **129**(3), e2023JF007352 (doi: https://doi.org/10.1029/2023JF007352), e2023JF007352 2023JF007352

Tsuji T, Johansen TA, Ruud BO, Ikeda T and Matsuoka T (2012) Surface-wave analysis for identifying unfrozen zones in subglacial sediments. *Geophysics*, **77**(3), EN17–EN27 (doi: 10.1190/geo2011-0222.1)

Vantassel J and Cox B (2022) SWprocess: a workflow for developing robust estimates of surface wave dispersion uncertainty. *Journal of Seismology*, **26**(4), 731–756

Veitch SA, Karplus M, Kaip G, Gonzalez LF, Amundson JM and Bartholomaus TC (2021) Ice thickness estimates of Lemon Creek Glacier, Alaska, from active-source seismic imaging. *Journal of Glaciology*, **67**(265), 824–832 (doi: 10.1017/jog.2021.32)

Walter F, Roux P, Roeoesli C, Lecointre A, Kilb D and Roux PF (2015) Using glacier seismicity for phase velocity measurements and Green's function retrieval. *Geophysical Journal International*, **201**(3), 1722–1737 (doi: 10.1093/gji/ggv069)

Yang J (2005) Rayleigh surface waves in an idealised partially saturated soil. *Geotechnique*, **55**(5), 409–414 (doi: 10.1680/geot.2005.55.5.409)

Zechmann JM, Booth AD, Truffer M, Gusmeroli A, Amundson JM and Larsen CF (2018) Active seismic studies in valley glacier settings: strategies and limitations. *Journal of Glaciology*, **64**(247), 796–810 (doi: 10.1017/jog.2018.69)

Zhang Z, Nakata N, Karplus M, Kaip G and Yi J (2022) Shallow ice-sheet composite structure revealed by seismic imaging near the west antarctic ice sheet (WAIS) divide camp. *Journal of Geophysical Research: Earth Surface*, **127**(12), e2022JF006777

APPENDIX A: ABBREVIATION SUMMARY

Table 2. List of Abbreviations Used Throughout the Manuscript

Initialism	**Full Description**
1-C	Single- or One-Component
3-C	Three-Component
MC	Multi-Component (regarding more than one component)
DC	Dispersion Curve
DP	Dispersion Panel
HVSR	Horizontal-to-Vertical Spectral Ratio
MASW	Multi-Channel Analysis of Surface Waves
P-wave	Compressional Wave
S-wave	Shear Wave
SV-wave	Vertical Shear Wave with particle motion parallel to plane of wave propagation
CC	Complex Conjugate (Component): $Z(d,t) + iR(d,t)$
R	Radial (Component) - along to source-receiver direction
T	Transverse (Component) - counter clockwise from R direction
Z	Vertical (Component)

746 # APPENDIX B: NOTATION SUMMARY

Table 3. List of Notations Used Throughout the Manuscript

Symbol	Description
V_p	Compressional-wave (P-wave) velocity
V_s	Shear-wave (S-wave) velocity
V_r	Rayleigh-wave phase velocity
ρ	Density
U_x	Horizontal particle displacement
U_z	Vertical particle displacement
Φ	Scalar potential associated with P-waves
Ψ	Vector potential associated with SV-waves
A	Amplitude scaling factor
p	Horizontal slowness
$\hat{\eta}_p$	Vertical slowness for P-waves: $\sqrt{1/V_r^2 - 1/V_p^2}$
$\hat{\eta}_s$	Vertical slowness for S-waves: $\sqrt{1/V_r^2 - 1/V_s^2}$
f	Frequency
f_0	Resonant (or fundamental) frequency
ω	Angular frequency: $2\pi f$)
λ	Wavelength: V_r/f
z	Depth
h	Ice thickness
h_r	Depth at which Rayleigh wave particle motion reverses (retrograde to prograde)
L	Array length
Δr_x	Receiver spacing
d	Source-receiver offset
t	Time
$D(d,t)$	Seismic data in shot-gather format
$D(d,\omega)$	Frequency-domain transform of seismic data
$D_N(d,\omega)$	Frequency-domain seismic with normalized trace amplitudes

SUPPLEMENTAL

S1. Generation of Rayleigh Waves

This section reviews Rayleigh wave theory using wavefield potentials (related to P- and S-waves) rather than the displacement wavefields commonly presented in textbooks. Although displacement-based formulations are widely used for their practical application in matrix methods for solving the wave equation (Aki and Richards, 2002), our approach follows Lay and Wallace (1995) and provides insight into the underlying principles of our MC approach to Rayleigh wave analysis.

Rayleigh waves exist in the near surface of an elastic medium due to the interference of elastic body waves (specifically, the P-SV wave system with S-wave particle motion polarized in the plane of wave propagation) and their conversions at the free surface such as the air-ice interface considered herein (Lay and Wallace, 1995; Liner, 2012). These two wave modes are coupled: when either wave interacts with a boundary with discontinuous material properties, the resulting reflection, refraction, and transmission effects occur in addition to wave-mode conversion (Fig. S1.1a). Fig. S1.1b illustrates this mechanism for an incident reflected PS wave striking the free surface at an angle j. Interaction of this wave mode with the free surface produces a twice-converted P wave (PSP) and a converted SV wave (PSS), that are respectively reflected at angles j and i and propagate with velocities V_p and V_s of the first layer.

Rayleigh waves are generated when the SV wave meets the free surface where surface tractions vanish at (and beyond) a critical angle. The incident SV wave is converted into a refracted P wave (propagating along the surface) and a 180° phase-shifted, post-critical reflection of SV wave energy (with near-vertical particle motion that grazes the surface) (Lay and Wallace, 1995). The respective wave-mode interactions with the free surface generate evanescent P- and SV-waves (Fig. S1.1c). The resulting P- and SV-wave displacements are described by the gradient of the scalar potential, Φ, and the curl of the vector potential, Ψ, respectively.

The simultaneous existence of these two out-of-phase modes generates a Rayleigh wave with elliptical particle motion (Lay and Wallace, 1995) that propagates along the surface (Fig.S1.1d). Rayleigh-wave vertical (U_z) and horizontal (U_x) displacements are represented by sums of spatial derivatives of the scalar and vector potentials of the evanescent wavefield (Φ_E and Ψ_E, respectively).

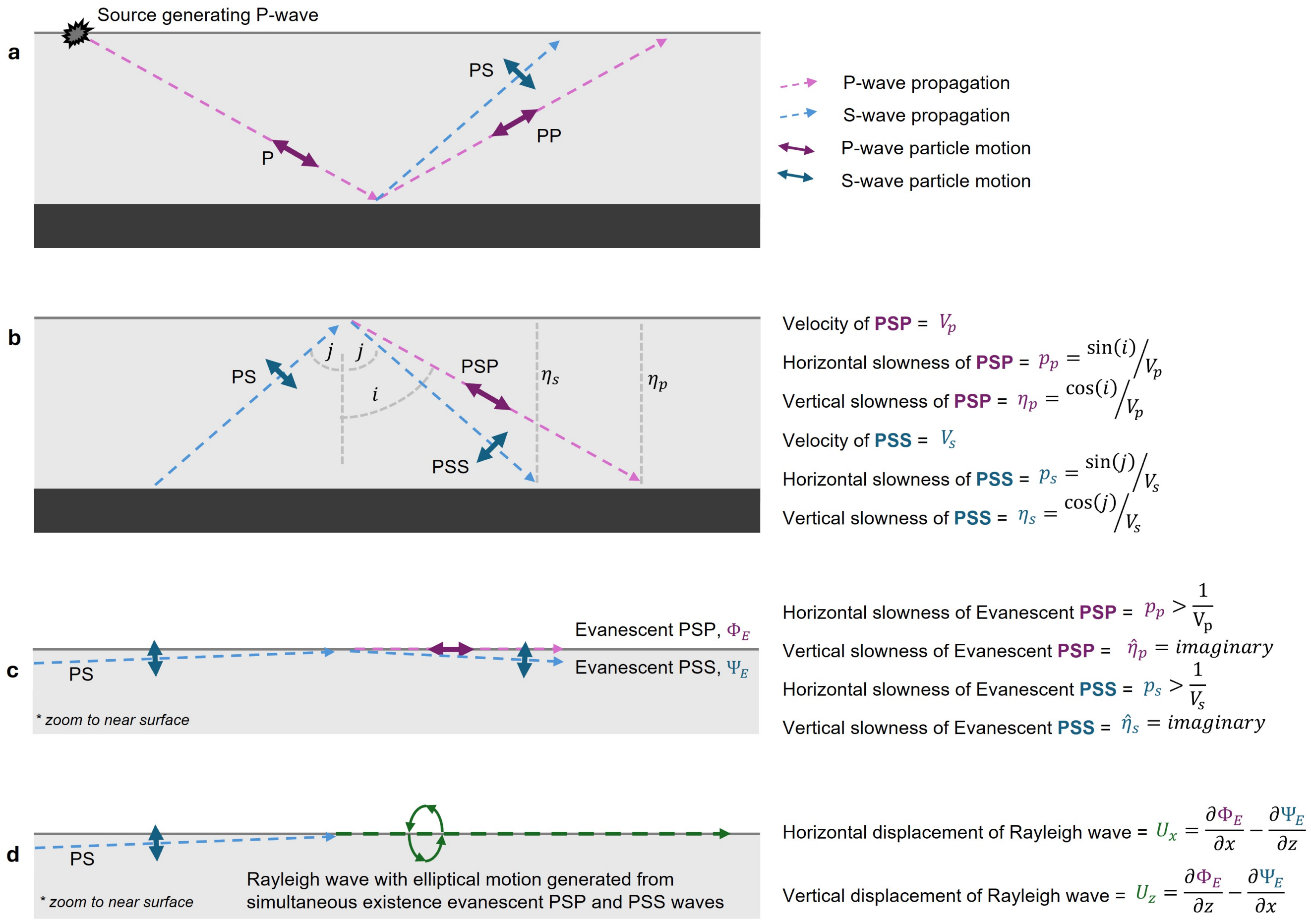

Fig. S1.1. Conceptual representation of Rayleigh-wave generation from a vertical impact source. (a) An incident P wave reflects off an impedance contrast producing up-going reflected P (PP) and S (PS) waves. (b) The up-going PS wave undergoes total internal reflection at the free surface producing a PSS wave and a mode-converted PSP wave. The velocity and horizontal and vertical slownesses are described relative to the free-surface incidence angle. (c) At large angles of incidence, evanescent PSP and PSS waves propagate along the surface out-of-phase producing (d) a Rayleigh wave with retrograde elliptical particle motion along the free surface. Components U_z and U_x are described in terms of the potentials, Φ and Ψ, of the evanescent wavefields. Note panels (c–d) zoom to the near-surface region of the conceptual model.

774 S2. Generation of Dispersion Panels

This section outlines the forward problem of constructing DPs from the seismic record. Quantifying the dispersion relation from seismic trace data requires decomposing the time-series signals into their frequency components. The *MASWaves* (Olafsdottir and others, 2018) implementation follows the method of Park and others (1998) in using slant-stacking of Fourier-transformed shot-gather seismic trace data. We describe the process visually in Fig. S2.1. Let $D(d_j, t)$ represent the seismic response at source-receiver offset d_j and time t, recorded from a source shot indexed by j (Fig. S2.1a1). When transformed into the frequency domain via Fourier transform (Fig. S2.1a2), the data become a complex function of angular frequency ω:

$$D(d_j, \omega) = |D(d_j, \omega)| e^{-i\phi_j}. \tag{6}$$

This representation contains terms associated with the magnitude $|D(d_j, \omega)|$ and phase ϕ_j. The prior incorporates amplitude variations due to factors such as geometrical spreading and energy loss. If the data are normalized to unity, then only the phase term is retained as:

$$D_{norm}(d_j, \omega) = e^{-i\phi_j}, \tag{7}$$

where $e^{-i\phi_j}$ encodes the dispersive behavior because

$$\phi_j = \frac{\omega(V_r) d_j}{V_r}. \tag{8}$$

The velocity dependence of different frequency components manifests as a systematic phase shift across the array and can be directly extracted (as shown in Fig. S2.1a3) from the frequency-domain signal via:

$$\phi_j = \arctan\left(\frac{\mathrm{Im}[D]}{\mathrm{Re}[D]}\right).$$

Although we parse the signal into phase and frequency components, these values are insufficient to resolve V_r (via Eqn. (8)) unless the velocity dependence on frequency is accurately modeled or validated. Our approach to resolving this ambiguity invokes a slant-stacking operation. A coherency measure is defined by integrating the product of the normalized data and the complex exponential of the test phase

ϕ_j^{test}:

$$D_{norm}(\phi_j^{\text{test}}, \omega) = \int D_{norm}(d_j, \omega) e^{i\phi_j^{\text{test}}}\, \mathrm{d}x. \tag{9}$$

This integral evaluates the similarity between the observed and test phase; that is, when the exponential terms align, the integrand is maximized (or, ideally, unity as D_{norm} is normalized) and this means that the V_r^{test} is physically plausible at that frequency. By assuming a trial velocity V_r^{test} and exploring a range of frequencies present in the data, one can compute a hypothetical phase (Fig. S2.1b1–b2):

$$\phi_j^{\text{test}} = \frac{\omega d_j}{V_r^{\text{test}}}$$

and calculate $e^{i\phi_j^{\text{test}}}$ (Fig. S2.1b3).

Repeating this analysis over all offsets (Fig. S2.1c1) and stacking the functions of f and V_r (Fig. S2.1c2) generates a DP from which the DC can be identified using the maximum values. Each “slant” (i.e., test velocity versus offset) represents a plane wave and the amplitudes are normalized by trace number prior to “stacking” the f-V_r panel.

S3. MC DC Sensitivity to Data Conditioning

This section outlines a recommended data-conditioning flow for shot gathers aimed at producing high-SNR DPs. Previous studies (e.g., Foti and others, 2018) emphasize the importance of interpolating missing traces, applying appropriate time windowing to capture the full Rayleigh-wave signal across all offsets, and muting the direct wave that can interfere with the Z-component. Here, we apply these steps consistently to both the Z and R components. We illustrate this workflow using the Saskatchewan Glacier dataset, beginning with the raw data (Fig. S3.1), followed by removal of the noisy zero-offset trace (Fig. S3.2). We then compare infilling the missing trace with a null trace versus interpolation (Fig. S3.3 and Fig. S3.4, respectively), and conclude with the fully conditioned gather after zero-offset trace removal, trace interpolation, and direct-wave muting (Fig. S3.5).

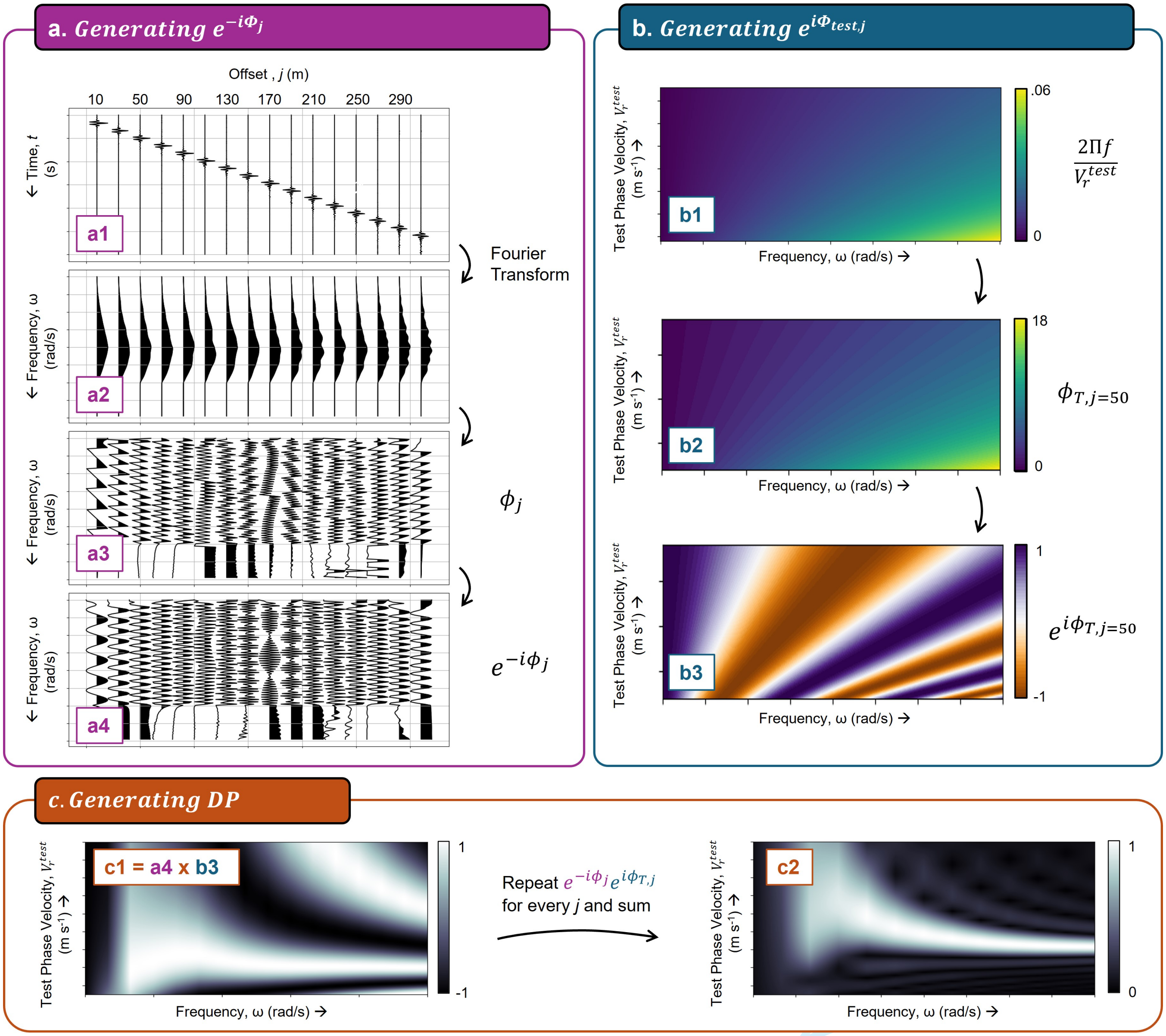

Fig. S2.1. Overview of the process used to generate dispersion panels (DPs) from shot-gather seismic data for extracting experimental dispersion curves (DCs). (a) Steps involved in calculating the first exponential term, derived from the complex phase of the frequency-transformed shot-gather. Every 20th trace is shown for clarity in all sub-panels. Sub-panel (a1) shows the input shot gather, $D(d_j, t)$; (a2) the frequency-domain representation of the input shot gather, $D(d_j, f)$; (a3) the extracted phase for each trace, ϕ_j; and (a4) the first exponential term, $\exp(i\phi_j)$. (b) Construction of the second exponential term computed from a range of test phase velocities c_T and frequencies. Sub-panel (b1) shows the computed matrix of $\frac{2\pi f}{V_r^{\text{test}}}$ for various V_r^{test} and f; (b2) the offset-scaled version of this matrix (a test phase, ϕ_T) for a representative trace at $j = 50$; and (b3) the second exponential term, $\exp(-i\frac{2\pi f d_j}{V_r^{\text{test}}})$, shown for $j = 50$. (c) Generating the final DP by (c1) computing the product of the two exponential terms for each offset; and (c2) stacking the result across offset.

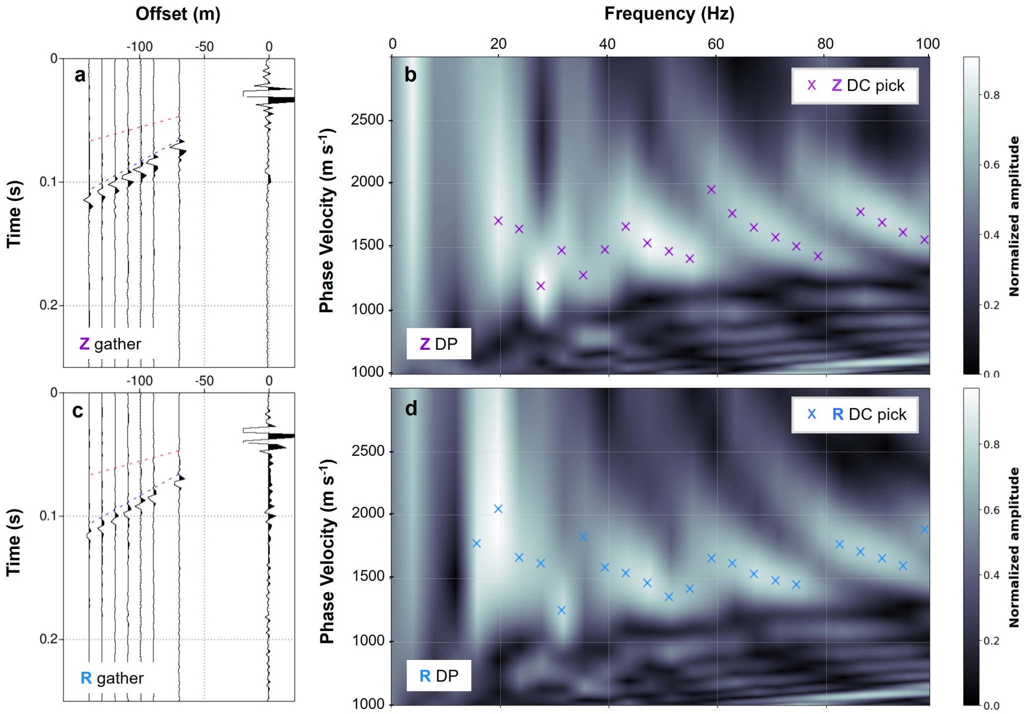

Fig. S3.1. Comparison of Z- and R-component shot gathers, DPs and associated DC picks where the data has no conditioning applied.

S4. MC DC Sensitivity to Acquisition Geometry

Practical limitations on survey design are often a restricting factor in geophysical field experiments. For example, active seismic experiments require transportation of a source (typically a sledgehammer), a base plate, and numerous geophones, and involve careful geophone deployment to ensure sufficient coupling and accurate positioning and potentially orientation, all of which can be challenging in glacial field conditions (Aster and Winberry, 2017). It is important to understand the practical limitations of survey design in order to make decisions about future field experiments or to improve the processing of existing data sets.

To illustrate the impact of different survey designs on both the negative and positive frequencies of the CC-DP, we use the synthetic ice-over-bedrock half-space model described in the main text. Starting from the idealized acquisition, we modify the geometry in two independent ways, assuming a total of 10 receivers to represent a weight-limited field expedition (e.g., helicopter-supported). In the first case, we prioritize array length (500 m) by increasing the receiver spacing to 50 m. In the second case, we prioritize spatial sampling by using a 10 m receiver spacing, which reduces the array length to 100 m. Figure S4.1 shows the corresponding DPs generated from conditioned data after applying direct-wave removal and

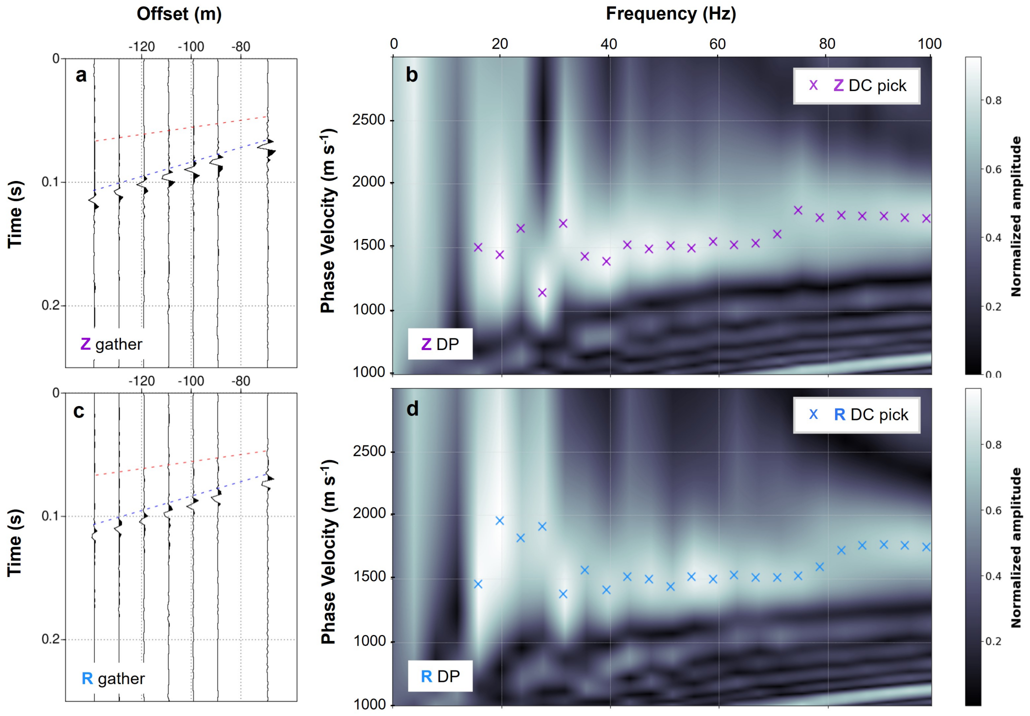

Fig. S3.2. Comparison of Z- and R-component shot gathers, DPs and associated DC picks where the zero-offset trace is removed.

offset-windowing, which yield more reliable results.

Greater receiver spacing (Fig. S4.1b) has a less critical impact on DP resolution than a short-aperture survey (Fig. S4.1c). Larger receiver spacing primarily limits the higher-frequency content; in this experiment, however, a 10 m spacing is not restrictive for resolving the 100 m-thick ice layer. In contrast, the shorter array suppresses low-frequency content, thereby reducing the maximum depth of investigation. For this model, a 100 m array length limits resolution of the ice–bedrock interface, as the DC lacks reliable low-frequency picks associated with dispersion at this interface.

Since prioritizing array aperture over receiver spacing is judicious for Rayleigh-wave dispersion analysis, a practical strategy is to set the receiver spacing to approximately half the shallowest depth of investigation while extending the total receiver array to include as many geophones as available. To further optimize offset coverage, denser shot spacing can be used; for example, with 20 m receiver spacing, initiating shots every 10 m yields data at 10 m offset intervals.

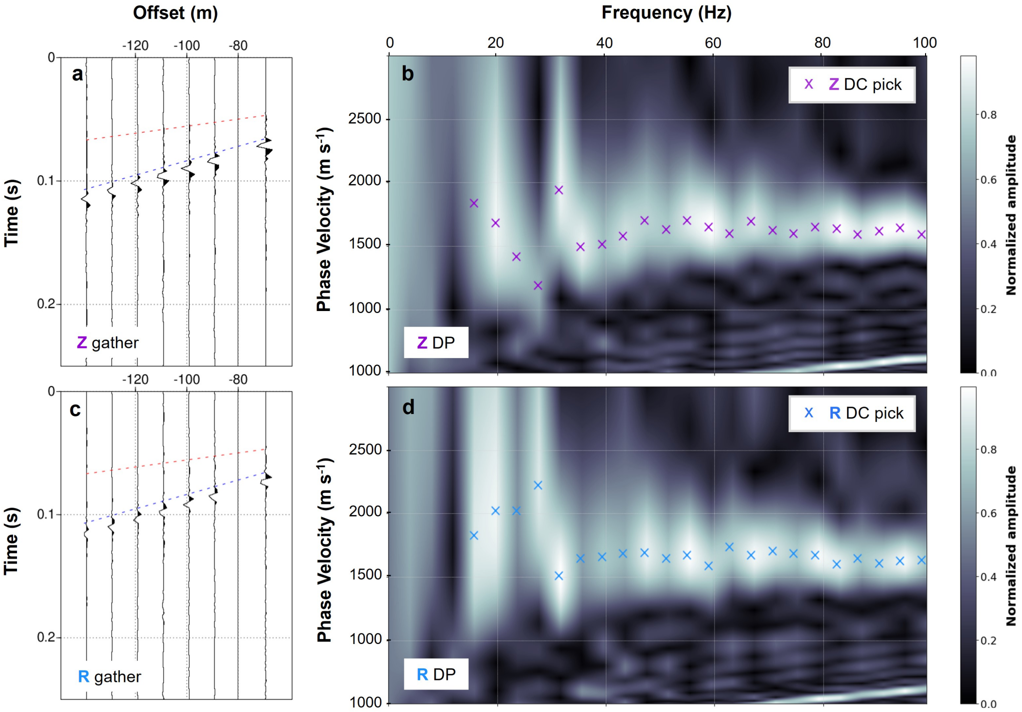

Fig. S3.3. Comparison of Z- and R-component shot gathers, DPs and associated DC picks where the zero-offset trace is removed and the missing trace at 80 m offset is infilled with a null trace.

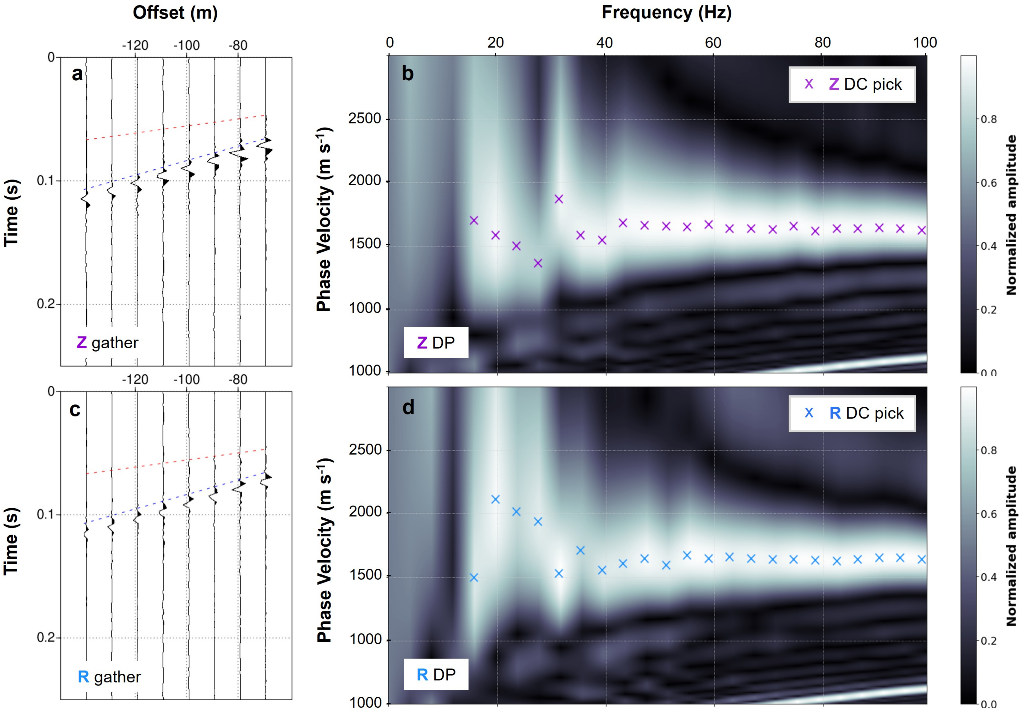

Fig. S3.4. Comparison of Z- and R-component shot gathers, DPs and associated DC picks where the zero-offset trace is removed and the missing trace at 80 m offset is interpolated.

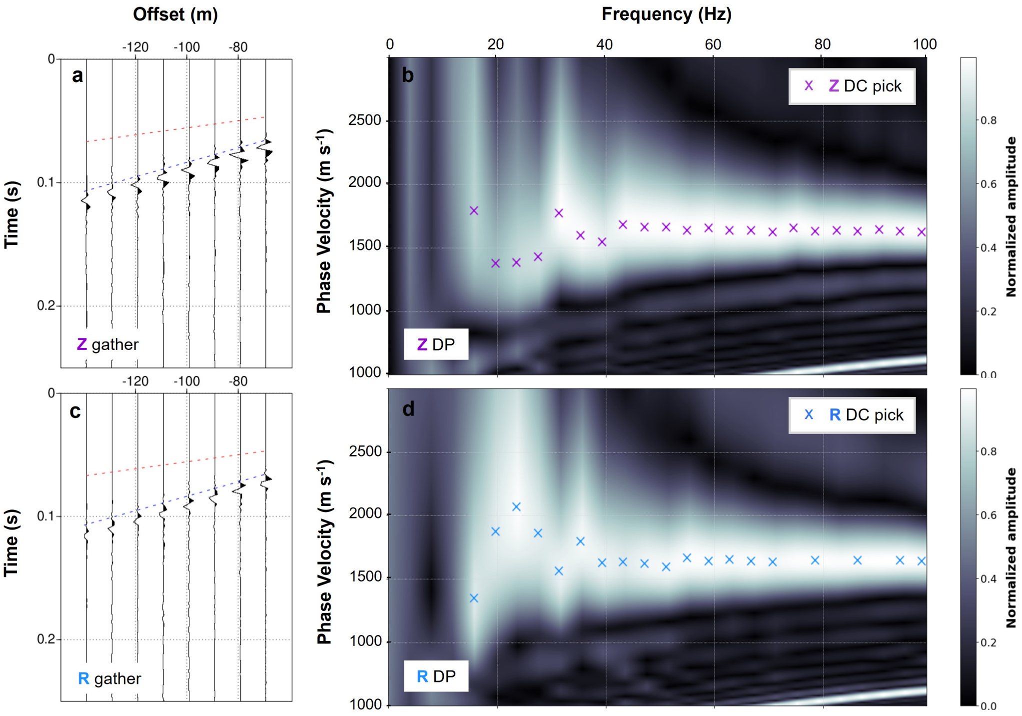

Fig. S3.5. Comparison of Z- and R-component shot gathers, DPs and associated DC picks where the zero-offset trace is removed, the missing trace at 80 m offset is interpolated and the direct wave is muted.

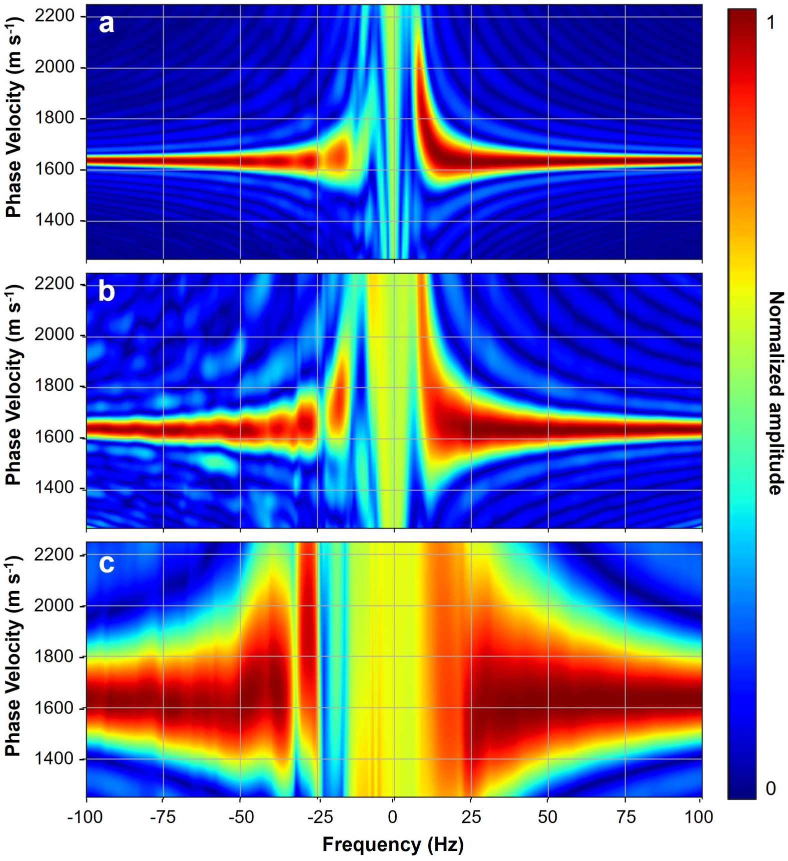

Fig. S4.1. DPs for the CC-component data from three acquisition designs over a two-layer ice–bedrock half-space model (interface at 100 m). The data were conditioned by removing the direct P-wave arrival and applying offset windowing to capture the full Rayleigh-wave signal across all offsets. (a) An idealized experiment with a long array (1000 m) and dense receiver spacing (1 m). Two additional experiments assume a total of 10 receivers: (b) sparse receiver sampling (50 m), resulting in a 500 m array length, and (c) denser receiver sampling (10 m), resulting in a shorter array length of 100 m. The sparse-receiver survey exhibits less distortion than the limited-aperture case.